Title
High Throughput Web Inspection System using Time-stretch Real-time Imaging

Permalink
https://escholarship.org/uc/item/7j4068cd

Author
Kim, Chanju

Publication Date
2013

Peer reviewed|Thesis/dissertation

UNIVERSITY OF CALIFORNIA

Los Angeles

High Throughput Web Inspection System using Time-stretch Real-time Imaging

A thesis submitted in partial satisfaction

of the requirements for the degree Master of Science

in Electrical Engineering

By

Chanju Kim

2013

ABSTRACT OF THE THESIS

High Throughput Web Inspection System using Time-stretch Real-time Imaging

by

Chanju Kim

Master of Science in Electrical Engineering

University of California, Los Angeles, 2013

Professor Bahram Jalali, Chair

Photonic time-stretch is a novel technology that enables capturing of fast, rare and non-repetitive events. Therefore, it operates in real-time with ability to record over long period of time while having fine temporal resolution. The powerful property of photonic time-stretch has already been employed in various fields of application such as analog-to-digital conversion, spectroscopy, laser scanner and microscopy [1-7]. Further expanding the scope, we fully exploit the time-stretch technology to demonstrate a high throughput web inspection system [8]. Web inspection, namely surface inspection is a nondestructive evaluation method which is crucial for semiconductor wafer and thin film production. We successfully report a dark-field web inspection system with line scan speed of 90.9 MHz

which is up to 1000 times faster than conventional inspection instruments. The manufacturing of high quality semiconductor wafer and thin film may directly benefit from this technology as it can easily locate defects with area of less than 10 μm × 10 μm where it allows maximum web flow speed of 1.8 km/s.

The thesis provides an overview of our web inspection technique, followed by description of the photonic time-stretch technique which is the keystone in our system. A detailed explanation of each component is covered to provide quantitative understanding of the system. Finally, imaging results from a hard-disk sample and flexible films are presented along with performance analysis of the system. This project was the first application of time-stretch to industrial inspection, and was conducted under financial support and with close involvement by Hitachi, Ltd.

The thesis of Chanju Kim is approved.

Tatsuo Itoh

Benjamin Williams

Bahram Jalali, Committee Chair

University of California, Los Angeles

2013

Table of Contents

LIST OF FIGURES

ACKNOWLEDGEMENTS

It is with greatest pleasure that I acknowledge the support and guidance of Professor Bahram Jalali. I would like to show my deepest gratitude to Professor Bahram Jalali especially for taking me in as a graduate student researcher and granting me with the exciting research opportunity and the creative lab environment. Besides my advisor, I sincerely appreciate my Master's thesis committee, Professor Benjamin Williams and Professor Tatsuoh Itoh of the UCLA Department of Electrical Engineering for their helpful revision and fruitful comments on my thesis. My sincere thanks also go to Professor Chao Wang, a former postdoctoral researcher in our group, as he guided me through the very first research project when I joined the laboratory. I would like to also thank Professor Keisuke Goda and Professor Kevin Tsia for their previous research as they provided foundation of my work. I share the credit of this work with my colleague and dear friend Akio, Jacky and Ata. Akio's sharp engineering insight, Jacky's creative approach and Ata's all-seeing leadership was indispensible throughout the work. I also consider it an honor to work with Ata, Peter, Brandon and David as they were great mentors who shared their insight on various research projects. I am also indebted to Eric, Mohammad, Cejo and Daniel for their delightful discussions and most helpful advices. I deeply appreciate all of my colleagues at the Photonics Laboratory at UCLA as every bit of their positive influence resides in this work.

I would also like to gratefully acknowledge Hitachi Corporation for their financial and technical support for the project.

Finally, I thank my family for everything.

Chapter 1 Introduction

1.1 Web Inspection System

Among nondestructive evaluation methods, a web inspection system is a widely employed instrument where its application stretches from defect detection to quality control for various manufacturing purposes [8, 9]. One of the most popular web inspecting methods operates with a light source and a camera with linear photodetector array [10, 11]. The system relies on charge-coupled device (CCD) or complementary metal oxide (CMOS) detectors. The light is illuminated onto a sample while detector array collects scattered light from defects on the surface. It is clear that the system is limited by frame rate of the CCD/CMOS line scan camera which is roughly up to 100 kHz.

Another web inspection technique is a scanning laser coupled with a single-pixel photodetector [12]. The laser beam sweeps along the line-scan direction which is perpendicular to web flow direction. When the scanning beam hits the defect, scattered light is collected by the detector along with the temporal information; the time slot which the signal appears carries information of the defect location. Here, the limitation comes from inertia of the mechanical laser scanner while the single-pixel photodetector in the system can support higher scan rate.
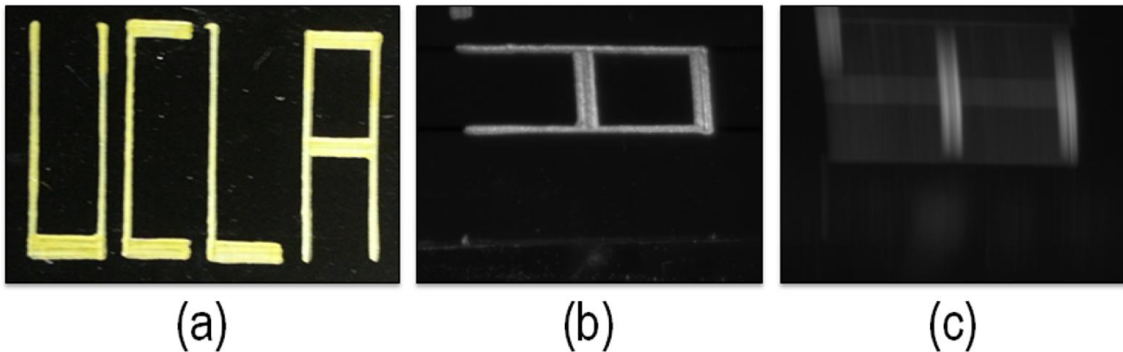
Figure 1-1. (a) UCLA written with metallic ink on an absorptive film, (b) CMOS camera image of stationary sample, (c) CMOS camera image of translating sample at the speed of 20 mm/s.
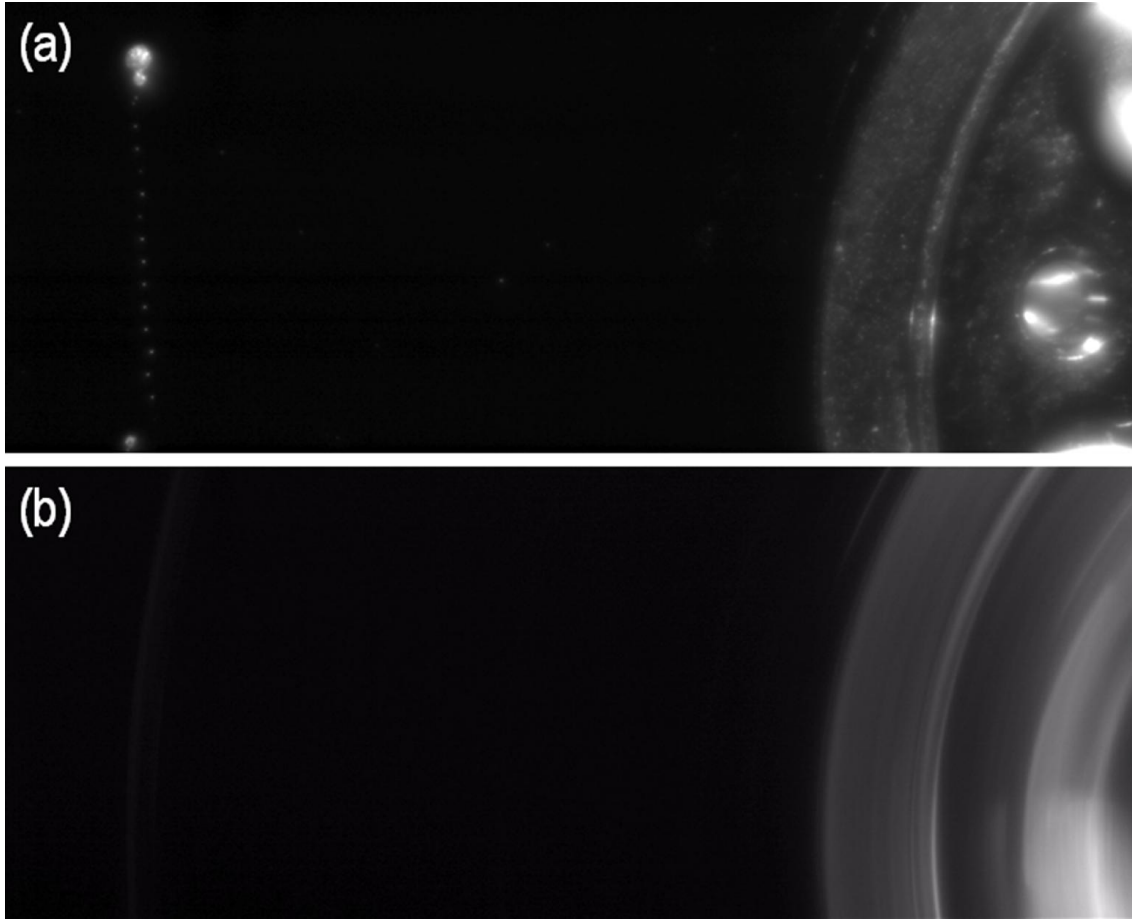
Figure 1-2. CMOS camera image of defects on hard-disk cylinder (a) stationary, (b) rotating at 7200 rpm. The blurring is evident in (b) where it illustrates the limitation of conventional CCD/CMOS-based inspection system at high flow speed.

It is important to note that these two types of conventional method have inherent scan speed limitation. Especially, in the first type, the CCD and CMOS device has its limitation imposed by fundamental trade-off relationship between sensitivity and speed. This scan speed bottleneck results in limited precision and application (Figure 1-1 (a) and Figure 1-2(b)). In addition, high-intensity illumination required in some CCD/CMOS system might cause damage to the sample under test. This study introduces a new modality in inspection and imaging: Time-Stretch Real-time Imaging, which allows 1,000 times higher scanning speed compared to other conventional inspection systems [6, 8].

1.2 Concept of Time-Stretch Real-time Imaging

Our real-time imaging system has two major steps in operation; which are 1) temporal dispersion (Group-velocity dispersion) and 2) spatial dispersion [6, 8]. The combination of two steps in operation allows us to achieve ultrafast imaging and inspection as mentioned from the previous section. Operation of the system starts with ultrafast pulse carrying broadband spectrum. The pulse is stretched in time where its spectrum is mapped into temporal waveform as shown in Figure 1-3. (a) and (b). To reiterate the first step, each wavelength of the broadband spectrum is assigned into its corresponding time slot in temporally dispersed pulse; thus it achieves photonic time-stretch (quantitatively described by dispersive Fourier transformation in Chapter 2). Here the time-stretch can be realized by passing the pulse through a conventionally available high group-velocity dispersion element. The pulse is then passed on to a spatially dispersive element which forms a 1D rainbow pulse in space as can be seen from Figure 1-3 (c) and (d). Here, it is important to note that the wavelength of the actual pulse is centered at 800 nm which is irrelevant to rainbow color depicted in the figures throughout the thesis.

The 1D rainbow beam is then incident onto a sample-under-test which the spatial information of the object is retrieved by a single-pixel photodetector. Each wavelength or time instant within the detected pulse carries transmitted or reflected signal from different position of the sample. The pulse keeping its temporal dispersion and having spatial dispersion is equivalent to line-scanning of an object with varying wavelength beam at different space and time. To clarify each steps again, the system performs wavelength-to-time conversion through time-stretch in Figure 1-3 (a, b) and wavelength-to-space conversion with spatial dispersion in Figure 1-3 (c, d). The successful conversion between three domains: wavelength, time and space, offers us spatially resolved information with a single pulse and a single-pixel photodetector connected to any real-time digitizer.
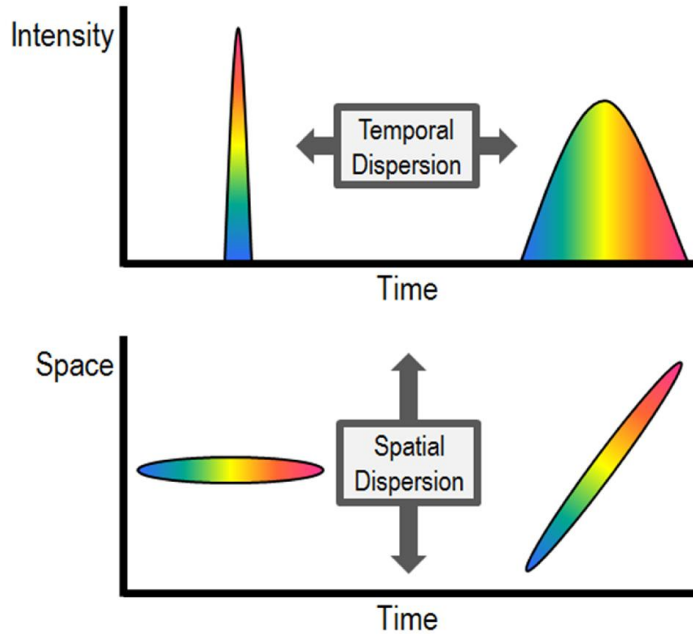
Figure 1-3. Description of two-step operation. (a) and (b) shows time-stretch where broadband pulse (a) is temporally dispersed mapping each wavelength into temporal waveform (b). (c) and (d) explain spatial dispersion where the time-stretched pulse (b, c) is spatially dispersed mapping each wavelength into space. (c) every wavelength is sharing the same space. (d) each wavelength occupies corresponding spatial coordinate.

1.3 Web Inspection System using Time-stretch Real-time Imaging

We propose and demonstrate a high throughput web inspection system exploiting time-stretch and utilizing the merits coming from dark-field imaging method (i.e., detecting low-contrast or transparent sample, and higher sensitivity to edges and boundaries of the sample). Also the dark-field imaging method completely blocks the DC term in the signal and minimizes the signal processing procedure which is advantageous compared to the bright-field analogue [8].

The complete schematic of the system is shown in Figure 1-4. The operation starts with a Ti:sapphire laser system which generates ultrafast broadband pulse having center wavelength at 800 nm with repetition rate of 90.9 MHz (11 ns of period). The pulse train is coupled into a dispersive fiber where the pulse is temporally dispersed. Group-velocity dispersion of -650 ps/nm is given for the fiber where the negative dispersion forces longer wavelengths to travel faster and shorter wavelengths to travel slower. The temporal

dispersion within the fiber maps each wavelength to its corresponding time slot which is equivalent to completing the photonic time-stretch. The time-stretched pulse is then spatially dispersed by a pair of diffraction gratings where each wavelength of the pulse is mapped into its corresponding coordinate within the 1D rainbow. The cylindrical lens focuses the 1D rainbow down to 20 μm allowing sharper spatial resolution in the web flow direction. The focused 1D rainbow beam is then incident onto the rotating sample. When the 1D rainbow is incident onto a clear surface, the rainbow will reflect back to the open space in a specular angle.
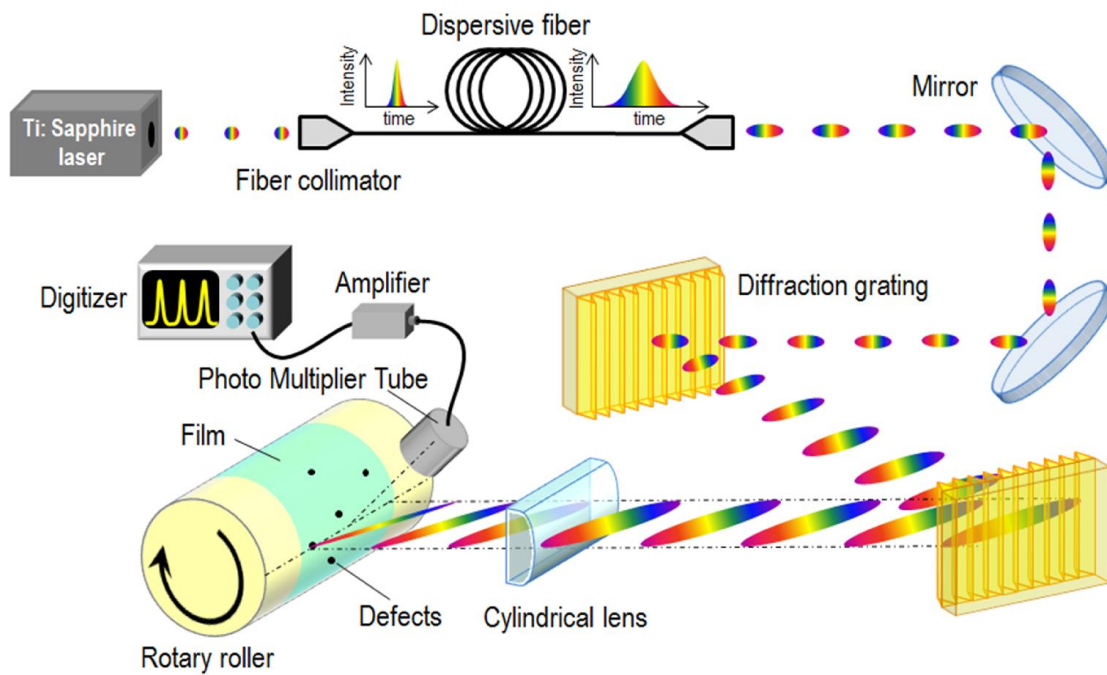
Figure 1-4. Schematic of the Web Inspection System

When a portion of the rainbow hits the defect as shown in Figure 1-5, the part of the rainbow beam that hit the defect will scatter into the photomultiplier tube. For example, as the yellow part of the rainbow has been scattered into the photomultiplier tube, the oscilloscope will show a signal peak at the time instant corresponding to yellow. A complete process of a single line scan has been performed and the position of the defect has been determined. By

extending the record time duration of oscilloscope, we can record series of line scans allowing us to reconstruct the scattering image for the sample-under-test.
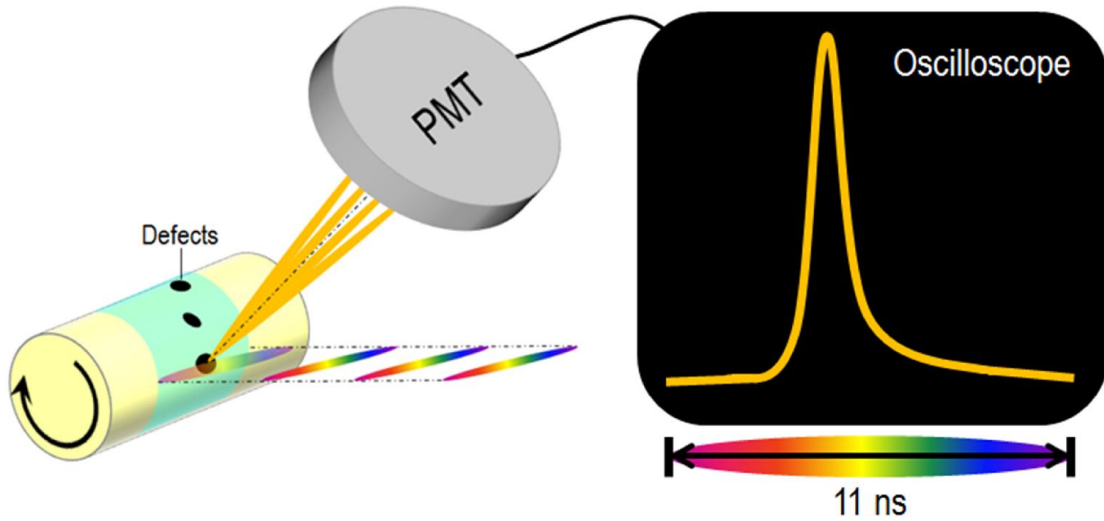
Figure 1-5. Operation description of the HDLS

If we focus on the light collection apparatus in the dark-field imaging technique, it is robust to misalignment since the optical signal collection is done by photodetector in open space. On the other hand, bright-field version of the system [8] requires total collection of the reflected lights where a minute vibration may require optical realignment of the entire system. Also, unlike our dark-field scanner, the bright-field system does not work effectively for the samples with low reflectivity. To summarize the section, we have successfully demonstrated dark-field inspection system with time-stretch real-time imaging technology which offers high-throughput inertia-free line scan. The results of this system will be shown in Chapter 4 which includes inspection images of flexible films and hard-disk drives.

Chapter 2 Background: Time-stretch in Real-time Imaging

As wavelength-to-time conversion by photonic time-stretch is one of the crucial steps in the system, this chapter will cover its principle and mathematically derive its operation. Here, the photonic time-stretch can be explained with more clarity and insight when it is described with the concept of dispersive Fourier transformation (DFT) [13, 14]. Therefore in this section we will use the term DFT as an equivalent of our photonic time-stretch operation. We will also cover its application to different type of photonic time-stretch based real-time imaging methods in section 2.3 and 2.4.

2.1 Time-stretch Dispersive Fourier Transformation

Whereas the photonic time-stretch technique is explained by the temporal dispersion of a pulse, a different conceptual approach for this same process is possible. Concept of the dispersive Fourier transformation (DFT) - synonymous to photonic time-stretch may start from spatial Fourier transformation which is regarded as one of the most important phenomena in Fourier optics and coherent optics. The DFT can be understood as an extension of this phenomenon where space-time duality of the light enables Fourier transformation in temporal domain [13, 15, 16]. By using a dispersive medium, it maps the spectrum of initial ultrafast optical pulse to a temporal waveform. Group-velocity dispersion in the dispersive element will temporally disperse the input pulse where the temporal envelope of the output pulse mirrors the spectrum (Figure 2-1). However, the pulse must go through sufficient temporal dispersion (i.e., longer propagation within the dispersive medium) so that each wavelength is well-separated in the time domain. This requirement is similar to far-field condition in spatial Fourier transformation, which is again imposed by space-time duality of the light [13, 17].
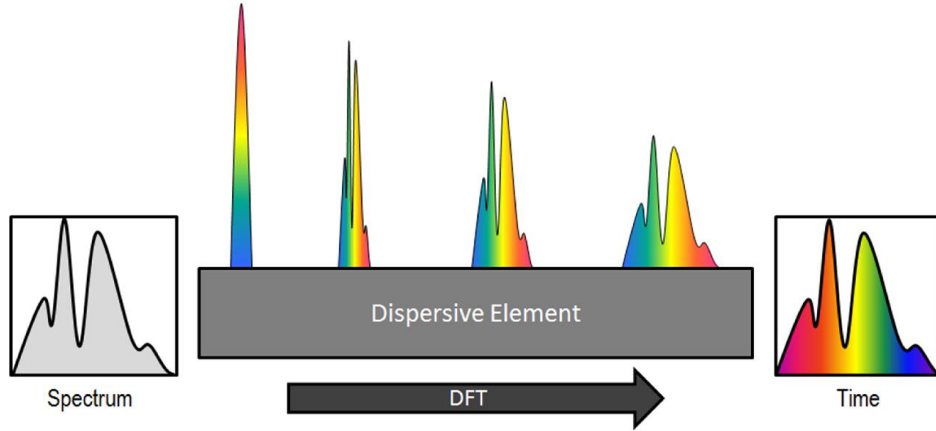
Figure 2-1. Photonic Time-stretch Dispersive Fourier Transformation (TS-DFT). When a pulse with spectrum shown in the left-side enters a dispersive element, group-velocity dispersion will perform dispersive Fourier transform where temporal waveform of the output pulse (right-side) will mirror the original spectrum.

The pulse with sufficient temporal dispersion is then captured by a high-speed single-pixel photodetector. Every time when the photodetector samples the temporal waveform, it is sampling the spectrum of original pulse. Therefore, the combination of a dispersive element and a photodetector allows real-time acquisition of spectrum for every pulse. This overcomes the speed limitations of traditional optical instruments achieving pulse-resolved spectroscopy [4, 6]. In this study, we combine the DFT process with the spatial dispersion to demonstrate ultrafast imaging of fast-moving samples.

2. 2 Mathematical formalism for dispersive Fourier transformation

The dispersive Fourier transformation for ultrafast imaging initially employed signal amplification through stimulated Raman scattering in parallel with the Fourier transformation [2, 18]. The amplified dispersive Fourier transformation (ADFT) provided image amplification and it is proven that the amplification is also possible for 800 nm regime [19]. Thus, for generality we derive a model for both ADFT (based on [18]) and DFT despite that our system does not have amplification process.

8

The goal of this section is to derive the coupled nonlinear Schrodinger equation that considers presence of multiple Raman amplification pump fields that starts from the Maxwell's wave equation [18, 20]. The resultant equation will prove that the quantitatively explained DFT operation in fact agrees with the mathematical formalism that is to be discussed.

When a pulse is propagating through an optical fiber, the total induced polarization $P(r, t)$ takes into account of the linear polarization $P_L(r, t)$, the noise-induced polarization $P_N(r, t)$, and the nonlinear polarization that consists of the Kerr effect $P_K(r, t)$ and the Raman effect $P_R(r, t)$. Thus the total induced polarization can be expressed as,

$$\mathbf{P}(r, t) = \mathbf{P_L}(\mathbf{r}, t) + \mathbf{P_N}(\mathbf{r}, t) + \mathbf{P_K}(\mathbf{r}, t) + \mathbf{P_R}(\mathbf{r}, t)$$

$$= \epsilon_0 \int_{-\infty}^{\infty} \chi_L(t - t') \mathbf{E}(r, t') dt'$$

$$+ \epsilon_0 \mathbf{E}(\mathbf{r}, t) \int_{-\infty}^{\infty} R_N(t - t') F_N(t') dt'$$

$$+ \epsilon_0 \mathbf{E}(\mathbf{r}, t) \left[\chi_K \mathbf{E}(\mathbf{r}, t) \cdot \mathbf{E}(\mathbf{r}, t) + \int_{-\infty}^{\infty} \chi_R \mathbf{E}(\mathbf{r}, t') \cdot \mathbf{E}(\mathbf{r}, t') dt' \right].$$

(1)

Where ϵ_0 is the permittivity of vacuum, χ_L is the linear susceptibility, F_N is a Langevin noise source that describes random molecular vibration of silica, R_N is the function that converts F_N into susceptibility, χ_K is the Kerr susceptibility and χ_R is the nonlinear susceptibility due to Raman scattering. Here we will neglect the noise-induced polarization term for simplicity and further description can be found in [20].

The total electric field can be expressed as,

$$\mathbf{E}(r, t) = \frac{1}{2} \hat{x} \left[\mathbf{E}_s(\mathbf{r}, t) e^{-i\omega_s t} + \mathbf{E}_p(\mathbf{r}, t) e^{-i\omega_p t} + c.c. \right].$$

(2)

As written above, with the polarization unit vector of $\hat{x}$, the electric field consists of the Stokes field $\mathbf{E}_s(\mathbf{r}, t)$ and the sum of the pump fields $\mathbf{E}_p(\mathbf{r}, t) = \sum_{j=1}^{\infty} \mathbf{E}_{p_j}$ where ω_s is the

9

carrier frequency of the Stokes field, and ω_p is the carrier frequency of the pump field. The Raman polarization $\mathbf{P}_R(r,t)$ is also described with Stokes and pump fields.

$$\mathbf{P}_R(\mathbf{r},t) = \frac{1}{2}\hat{x}\left[\mathbf{P}_{R_S}(\mathbf{r},t)e^{-i\omega_s t} + \boldsymbol{P}_{R_p}(\mathbf{r},t)e^{-i\omega_p t} + c.c.\right].$$

(3)

From (Eq. 2) we can obtain $\mathbf{E}\cdot\mathbf{E}$ which can be written as

$$\mathbf{E}\cdot\mathbf{E} = \frac{1}{2}|E_S|^2 + \frac{1}{2}|E_p|^2 + \frac{1}{2}E_p^*E_S e^{i(\omega_p-\omega_S)t} + \frac{1}{2}E_p E_S^* e^{-i(\omega_p-\omega_S)t} + \frac{1}{2}E_p E_S e^{i(\omega_p+\omega_S)t} +$$

$$\frac{1}{2}E_p^*E_S^* e^{-i(\omega_p+\omega_S)t} + \frac{1}{4}E_p^2 e^{-i2\omega_p t} + \frac{1}{4}E_p^{*2} e^{i2\omega_p t} + \frac{1}{4}E_S^2 e^{-i2\omega_S t} + \frac{1}{4}E_S^{*2} e^{i2\omega_S t}.$$

(4)

In the equation above, we regard only the first four terms since the rest of the term requires phase-matching of fields. Substituting (Eq. 4) into (Eq. 2) and then into (Eq.3) allows us to express the Raman polarization as,

$$\mathbf{P}_R^S(r,t) = \frac{1}{4}\epsilon_0 E_S(t)\int_{-\infty}^{\infty}\chi_R(t-t')\left[|E_S(t')|^2 + \sum_{j=1}^{\infty}\left|E_{p_j}(t')\right|^2\right]dt'$$

$$+ \frac{1}{2}\epsilon_0\sum_{j=1}^{\infty}E_{p_j}(t)\int_{-\infty}^{\infty}\chi_R(t-t')E_S(t')E_{p_j}^*(t')e^{-i\left(\omega_S-\omega_{p_j}\right)(t'-t)}dt',$$

(5)

where we drop the $\mathbf{r}$ dependence for convenience. Also, pump-pump couplings are ignored since their response is much weaker than Stokes-pump coupling in our case [20].

We then cast Maxwell's equation as,

$$\nabla^2\mathbf{E} - \frac{1}{c^2}\frac{\partial^2\mathbf{E}}{\partial t^2} = \mu_0\frac{\partial^2\mathbf{P}}{\partial t^2}.$$

(6)

Where c is the speed of light in vacuum μ_0 is the permeability of the vacuum, E is the total electric field and $\mathbf{P}$ is the total induced polarization. The expression of Stokes and pump

10

electric field can be divided into amplitude envelope $A(z,t)$ and cross-sectional distribution of the electric field $T(x,y)$. We may approximate $T_S(x,y)$ and $T_{p_j}(x,y)$ is equal in a single mode fiber; therefore the expression for Stokes and pump electrical field is given as,

$$\mathbf{E}_S(\mathbf{r},t) = T(x,y)A_S(z,t)e^{i\beta_0^S z},$$

$$\mathbf{E}_{p_j}(\mathbf{r},t) = T(x,y)A_{p_j}(z,t)e^{i\beta_0^{p_j} z}.$$

$$(7)$$

The field can be normalized through introduction of k_S^2 and $k_{p_j}^2$ as,

$$u_s(z,t) = k_s A_s(z,t)\sqrt{\int_{-\infty}^{\infty} T^2(x,y)dxdy},$$

$$u_{p_j}(z,t) = k_{p_j} A_{p_j}(z,t)\sqrt{\int_{-\infty}^{\infty} T^2(x,y)dxdy},$$

$$(8)$$

where,

$$k_S^2 = \frac{1}{2}n_s\sqrt{\frac{\epsilon_0}{\mu_0}}, k_{p_j}^2 = \frac{1}{2}n_{p_j}\sqrt{\frac{\epsilon_0}{\mu_0}}.$$

$$(9)$$

Here, n_s and n_{p_j} are the linear index of refraction at each Stokes and pump frequency respectively. Furthermore, we can express nonlinear coefficient γ_s, γ_{p_j} by Kerr and Raman susceptibility as,

$$\gamma_s = \frac{\omega_s n_2^S}{cA_{eff}k_S}, \gamma_{p_j} = \frac{\omega_{p_j} n_2^{p_j}}{cA_{eff}k_{p_j}}.$$

$$(10)$$

where A_{eff} is given as,

$$A_{eff} = \frac{\left(\int_{-\infty}^{\infty}\int_{-\infty}^{\infty} T^2(x,y)dxdy\right)^2}{\int_{-\infty}^{\infty}\int_{-\infty}^{\infty} T^4(x,y)dxdy}$$

$$(11)$$

11

Nonlinear refractive index n_2^S and $n_2^{p_j}$ can be written as,

$$n_2^S = \frac{3}{8n_s}\chi_k\left(1+\frac{2\chi_R^0}{3\chi_k}\right), \qquad n_2^{p_j} = \frac{3}{8n_{p_j}}\chi_k\left(1+\frac{2\chi_R^0}{3\chi_k}\right),$$

(12)

where χ_R^0 normalizes the Raman response function as,

$$\chi_R(t) = \chi_R^0 h_R(t),$$

(13)

while h_R satisfies $\int_{-\infty}^{\infty} h_R(t)dt = 1$.

Now we go back to Maxwell's equation, Eq. (6) to derive coupled nonlinear Schrodinger equation by working in frequency domain [20]. We take the Fourier transform of the electric field Eq. (7) substituted by Eq. (2) and the polarization given as Eq. (5). With slowly varying envelope approximation condition (~10 fs), resulting coupled equation for the Stokes wave is given as,

$$\frac{\partial u_S}{\partial z} - i\sum_{m=1}^{\infty}\frac{i^m\beta_m}{m!}\frac{\partial^m u_S}{\partial t^m} + \frac{\alpha_S}{2}u_S$$

$$= i\gamma_S(1-f_R)u_S\left[|u_S(t)|^2 + 2\sum_{j=1}^{\infty}\left|u_{p_j}(t)\right|^2\right]$$

$$+ i\gamma_S f_R u_S\int_{-\infty}^{\infty}h_R(t-t')\left[|u_S(t)|^2 + \sum_{j=1}^{\infty}\left|u_{p_j}(t)\right|^2\right]dt'$$

$$+ i\gamma_S f_R\sum_{j=1}^{\infty}u_{p_j}\int_{-\infty}^{\infty}h_R(t-t')u_S(t')u_{p_j}^*(t')\cdot e^{-i\left(\omega_{p_j}-\omega_S\right)(t-t')}dt'$$

(14)

Here, the fraction of the nonlinearity due to molecular vibration is $f_R = \left(1+\frac{3\chi_K}{2\chi_0}\right)^{-1}$[20]. The first term of Eq. (14) describes envelope evolution over distance, the second term represents dispersion effect on the wave and the third term is responsible for optical loss

12

while propagating. On the right hand side of the equation, the first term describes Kerr-induced self-phase modulation and cross-phase modulation. The second term in right hand side is molecular contribution to self-phase modulation and cross-phase modulation and the final term represents Raman amplification.

Equation 14 can be further simplified for picosecond regime which becomes,

$$\frac{\partial u_S}{\partial z} - i \sum_{m=1}^{\infty} \frac{i^m \beta_m}{m!} \frac{\partial^m u_S}{\partial t^m} + \frac{\alpha_S}{2} u_S$$

$$= i\gamma_S(1 - f_R)u_S \left[|u_S(t)|^2 + 2 \sum_{j=1}^{\infty} \left| u_{p_j}(t) \right|^2 \right]$$

$$+ i\gamma_S f_R u_S \left[|u_S(t)|^2 + \sum_{j=1}^{\infty} \left| u_{p_j}(t) \right|^2 \right] \int_{-\infty}^{\infty} h_R(t - t')dt'$$

$$+ i\gamma_S f_R u_S(t') \sum_{j=1}^{\infty} \left| u_{p_j} \right|^2 \int_{-\infty}^{\infty} h_R(t - t') \cdot e^{-i(\omega_{p_j} - \omega_S)(t - t')} dt'$$

$$(15)$$

Here, the first integral in the equation is equal to 1 because the response function is normalized. The second integral term is Fourier transform of the Raman response function which is,

$$\tilde{h}_R\left(\omega_{p_j}\right) = \int_{-\infty}^{\infty} h_R(t - t')e^{-i(\omega_{p_j} - \omega_S)(t - t')} dt'.$$

Eq. 15 is again reduced to

$$\frac{\partial u_S}{\partial z} - i \sum_{m=1}^{\infty} \frac{i^m \beta_m}{m!} \frac{\partial^m u_S}{\partial t^m} + \frac{\alpha_S}{2} u_S$$

$$= i\gamma_S u_S \left[|u_S(t)|^2 + (2 - f_R) \sum_{j=1}^{\infty} \left| u_{p_j}(t) \right|^2 \right] + i\gamma_S f_R u_S(t) \sum_{j=1}^{\infty} \left| u_{p_j} \right|^2 \tilde{h}_R(\omega_{p_j})$$

$$(16)$$

where the real part of $\tilde{h}_R(\omega_{p_j})$ describes Raman-induced index changes and imaginary part is responsible for the Raman gain. $\tilde{h}_R(\omega_{p_j})$ being symmetric function and assuming pump fields are much stronger than Stokes field, we can write Eq. 16 as,

$$
\frac{\partial u_S}{\partial z} - i \sum_{m=1}^{\infty} \frac{i^m \beta_m}{m!} \frac{\partial^m u_S}{\partial t^m} + \frac{\alpha_S}{2} u_S
$$

$$
= i\gamma_S u_S \sum_{j=1}^{\infty} 2 + f_R Re\left[\tilde{h}_R\left(\omega_{p_j}\right)\right] - f_R] \left|u_{p_j}(t)\right|^2
$$

$$
+ \gamma_S f_R u_S \sum_{j=1}^{\infty} \left|u_{p_j}\right|^2 Im\left[\tilde{h}_R\left(-\omega_{p_j}\right)\right].
$$

(17)

We turn Eq. (17) into frequency domain with assumption of undepleted pump fields thus regarding u_{p_j} as constants independent from time and position.

$$
\frac{1}{2\pi} \int_{-\infty}^{\infty} d\omega \left\{ \frac{\partial}{\partial z} - i \sum_{m=1}^{\infty} \frac{\beta_m}{m!} (\omega - \omega_S)^m + \frac{\alpha_S}{2} - i\gamma_S \sum_{j=1}^{\infty} [f_R Re\left[\tilde{h}_R\left(\omega_{p_j}\right)\right] - f_R] \left|u_{p_j}(t)\right|^2 \right.
$$

$$
\left. - \gamma_S f_R \sum_{j=1}^{\infty} \left|u_{p_j}(t)\right|^2 Im\left[\tilde{h}_R\left(-\omega_{p_j}\right)\right] \right\} \tilde{u}_S(\omega - \omega_S) e^{-i(\omega - \omega_S)t} = 0.
$$

(18)

The solution for Eq (18) is given as,

$$
\tilde{u}_S(z, \omega - \omega_S) = exp\left\{ i \sum_{m=1}^{\infty} \frac{\beta_m}{m!} (\omega - \omega_S)^m z - \frac{\alpha_S}{2} z + i\gamma_S \sum_{j=1}^{\infty} [f_R Re\left[\tilde{h}_R\left(\omega_{p_j}\right)\right] - f_R] \left|u_{p_j}\right|^2 z \right.
$$

$$
\left. + \gamma_S f_R \sum_{j=1}^{\infty} \left|u_{p_j}\right|^2 Im\left[\tilde{h}_R\left(-\omega_{p_j}\right)\right] z \right\}.
$$

(19)

We substitute Eq. (19) into Fourier transformation of the Stoke field given below,

14

$$u_S(z,t) = \frac{1}{2\pi} \int_{-\infty}^{\infty} \tilde{u}_S(z, \omega - \omega_S) e^{-i(\omega - \omega_S)t} d\omega.$$

(20)

Thus, the generalized amplified dispersive Fourier transformation is written as,

$$\tilde{u}_S(z,t) = \frac{1}{2\pi} \int_{-\infty}^{\infty} d\omega \, \tilde{u}_S(0, \omega - \omega_S) exp\left\{ i \sum_{m=1}^{\infty} \frac{\beta_m}{m!} (\omega - \omega_S)^m z - \frac{\alpha_S}{2} z \right.$$

$$+ i\gamma_S \sum_{j=1}^{\infty} \left[2 + f_R Re\left[\tilde{h}_R\left(\omega_{p_j}\right)\right] - f_R \right] \left|u_{p_j}\right|^2 z + \gamma_S f_R \sum_{j=1}^{\infty} \left|u_{p_j}\right|^2 Im\left[\tilde{h}_R\left(-\omega_{p_j}\right)\right] z$$

$$\left. - i(\omega - \omega_S)t \right\}$$

(21)

The equation above illustrates the original Stokes field spectrum $\tilde{u}_S(0, \omega - \omega_S)$ mapping to temporal waveform of $\tilde{u}_S(z,t)$. Assuming flat Raman gain spectrum, $Re\left[\tilde{h}_R\left(\omega_{p_j}\right)\right] \approx 0$ and $\sum_{j=1}^{\infty} \left|u_{p_j}\right|^2 Im\left[\tilde{h}_R\left(-\omega_{p_j}\right)\right]$ = constant, we can approximate Eq. (21) as,

$$u_S(z,t) \cong \frac{1}{2\pi} exp\left[-\frac{\alpha_S}{2} z + i\gamma_S \sum_{j=1}^{\infty} (2 - f_R) \left|u_{p_j}\right|^2 z + \frac{g_S}{2} z \right]$$

$$\cdot \int_{-\infty}^{\infty} \tilde{u}_S(0, \omega - \omega_S) exp\left\{ i \sum_{m=2}^{\infty} \frac{\beta_m}{m!} (\omega - \omega_S)^m z - i(\omega - \omega_S)T \right\} d\omega.$$

(22)

Here we have defined g_S and T as,

$$g_S = 2\gamma_S f_R \sum_{j=1}^{\infty} \left|u_{p_j}\right|^2 Im\left[\tilde{h}_R\left(-\omega_{p_j}\right)\right], \qquad T = t - \beta_1 z$$

(23)

15

As our web inspection system operates without the amplification from the pump field, we may drop u_{p_j} terms from Eq. (22). Also for our convenience, we ignore high-order dispersion coefficients. As a result, we can write the intensity profile as,

$$|u(z,T)|^2 = \left(\frac{1}{2\pi}\right)^2 e^{(g-\alpha)z} \left| \int_{-\infty}^{\infty} \tilde{u}_S(0, \omega - \omega_S) exp\left\{\frac{i\beta_2 z}{2}\left(\omega - \frac{\omega_0 T}{\beta_2 z}\right)^2\right\} d\omega \right|^2$$

(24)

For large value of GVD or $\beta_2 z$, the integrand in Eq. (24) oscillates rapidly in the frequency domain except at $\omega = \omega_0 + \frac{T}{\beta_2 z}$ which the phase vanishes [18]. In this regime, $T = \beta_2 z(\omega - \omega_0)$ holds and we substitute it into Eq. (24) giving out a more simplified intensity profile as below [13].

$$|u(z,T)|^2 = \frac{2}{\pi\beta_2 z} e^{(g-\alpha)z} \left| \tilde{u}\left(0, \frac{T}{\beta_2 z}\right) \right|^2.$$

(25)

Eq. (25) evidently shows that temporal intensity $|u(z,T)|^2$ is proportional to original spectrum of $\left| \tilde{u}\left(0, \frac{T}{\beta_2 z}\right) \right|^2$.

2.3 Serial time-encoded amplified microscopy

Serial time-encoded amplified microscopy (STEAM) [4] has the same two step operation: (1) temporal dispersion and (2) spatial dispersion as our system described in section 1.2 and 1.3. However, the operating order is different as it is explained here. The STEAM starts with the spatial dispersion of the ultrafast pulse where it is then directly incident on to the sample. Accordingly, the spatial information of the sample is stamped into the spectrum of the reflected beam. The spatially dispersed beam reflected from the sample is then collected and goes through DFT by a dispersive element which is being pumped by additional light source. Here, the spectrum-encoded pulse is amplified by stimulated Raman scattering in addition

to DFT which the step as a whole is named ADFT. The resultant pulse is acquired by a single-pixel photodetector and the image of the sample is reconstructed. Through this technique, fast dynamics of a laser ablation process could be observed in detail [4] and imaging microfluidic flow of circulating tumor cells at flow speed of 4 m/s was possible [21]. It should be also noted that two-dimensional spatial imaging is performed with orthogonally orientated 2D spatial dispersers which consists of a virtually imaged phased array and a diffraction grating.

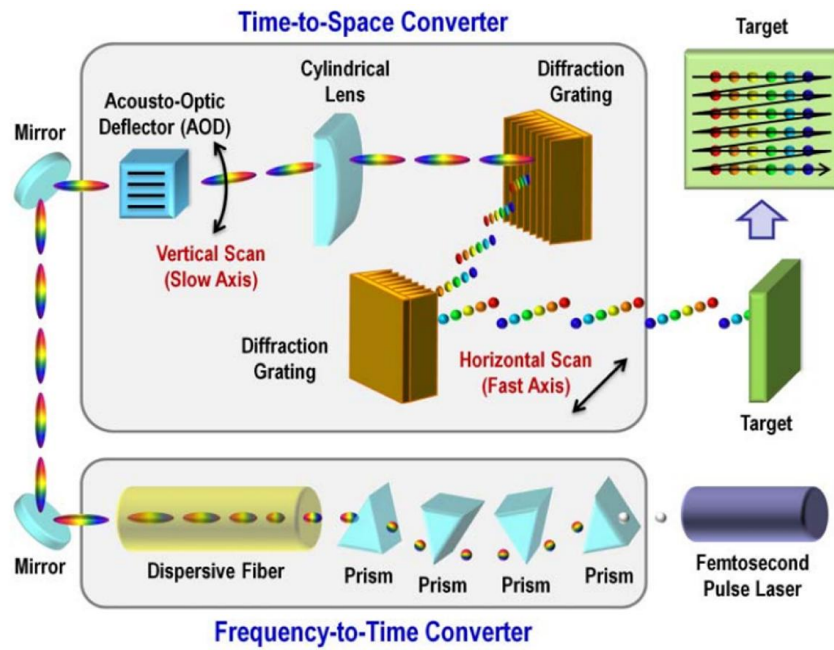2.4 Hybrid Dispersion Laser Scanner

Figure 2-2. Schematic of HDLS [6]

Comparing Figure 1-4 and Figure 2-2, Hybrid Dispersion Laser Scanner (HDLS) [6] has the same operation order as our system. It first performs DFT through a dispersive fiber, mapping the wavelength of an ultrafast pulse into time. The spatial dispersion is employed by a pair of diffraction grating which maps the wavelength into space (1D rainbow beam). The Figure 2-2 shows that the schematic is similar to our system except that it may include acousto-optic deflector (AOD). The AOD allows 2D raster scanning of a sample by deflecting

17

the beam in vertical direction while the diffraction grating realizes scanning in horizontal direction. Through HDLS, 2D reflection imaging, sub-nanometer-scale surface vibrometry [22], and high-precision flow cytometry with flow speed of 1 m/s was successfully demonstrated.

Chapter 3 Setup

In this section, our real-time web inspection system and its components will be described in detail. Starting from ultrafast pulse laser where the initial pulse is generated, then dispersive fiber, diffraction grating, sample, photodetector, and oscilloscope will be covered.

3.1 Ultrafast Pulse Laser

Front-end of the inspection system is a mode-locked Titanium Sapphire Laser System (KM Lab) which produces pulse with approximately 40 fs of pulse width, center wavelength set as 800nm, 23 nm of bandwidth and repetition rate of 90.9 MHz. To achieve maximum field of view, it is important to tune the cavity for maximum spectral bandwidth.

From the trigger signal of our laser system shown in Figure 3-1., we can confirm that the pulse repetition rate is 90.9 MHz with approximately 11 ns of pulse repetition period. It is important to note that the scan rate, R, is determined by the pulse repetition rate of the laser. We may notice in the later part that the laser trigger signal is crucial in the image reconstruction stage.
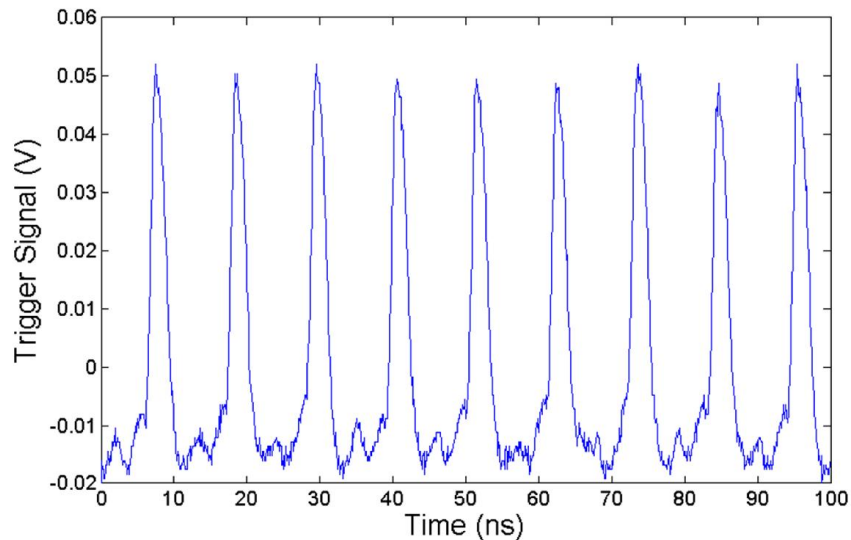

Figure 3-1. Laser trigger signal. The signal has repetition rate of 90.9 MHz (period of 11 ns) indicating repetition rate of the laser pulse.

3.2 Dispersive Fiber

Dispersive fiber is the element that realizes time-stretch/DFT in our system. Generally, the process can be achieved by standard single-mode fibers including long-haul transmission fibers and dispersion-compensation fibers (DCFs). Also slightly different elements such as chirped fiber Bragg gratings or chromo-modal dispersion in DCFs are compatible. However, multi-mode fibers (MMFs) do not operate well with the DFT where the modal dispersion in addition to GVD enhances the ambiguity in the wavelength-to-time mapping process.

The pulse repetition rate of 11 ns imposes upper limit of the temporal dispersion amount. If the initial pulse is stretched more than the 11 ns window of our pulse repetition period, the DFT processed pulses will overlap with each other (Figure 3-2). This causes multiple wavelength components during the overlapping instant. Thus in ideal case, GVD of the fiber should be carefully selected to avoid the overlapping by abiding to the next simple rule.

The pulse duration after temporal dispersion can be expressed as $\Delta\tau = |D|\Delta\lambda$, where D is the GVD of the fiber. The dispersive fiber and the laser system should meet the following condition $\Delta\tau < \frac{1}{R}$. Here $\frac{1}{R}$ is the pulse repetition period.
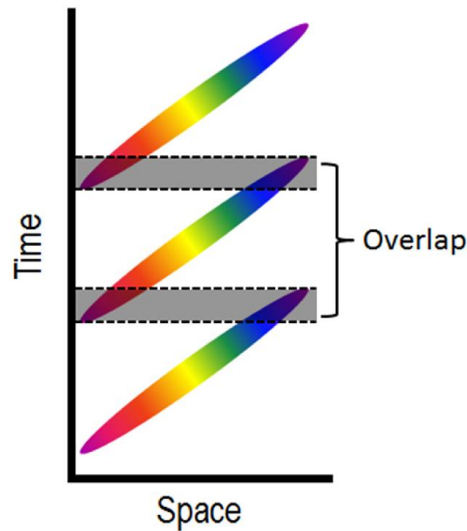

Figure 3-2. Pulse train of the rainbow beam overlapping with consecutive pulses. The overlap arises when laser repetition rate or GVD is excessive.

The group-velocity dispersion of our single-mode dispersive fiber is given as -650 ps/nm. Accordingly, the pulse duration for our system can be calculated, $\Delta\tau = |D|\Delta\lambda = 650$ ps/nm × 23 nm ≈ 15 ns, which exceeds the repetition period of our laser (11 ns). As a solution for this issue, we have spatially blocked the overlapping part of the rainbow beam which sacrifices field-of-view in our system.
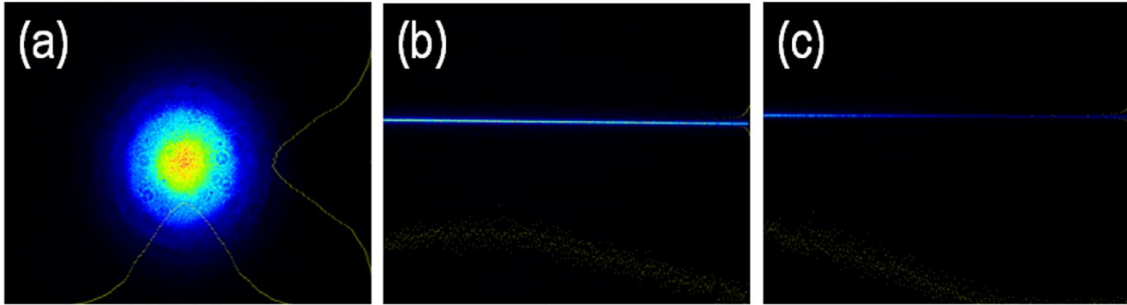
3.3 Diffraction Grating and Polarizer

Figure 3-3. Beam profile of (a) pulse before the diffraction gratings, (b) pulse after the diffraction gratings. (c) shows non-uniform rainbow beam profile illustrating polarization dependency of the diffraction grating.
Beam width: (a) 1.5 mm (H) × 1.5 mm (V), (b and c) 3 cm (H) × 19.8 μm.

The temporally dispersed pulse with beam waist of 1.5 μm (Figure 3-3 a) is then passed onto diffraction gratings for spatial dispersion realizing 1D rainbow beam (Figure 3-3 b). We use a pair of diffraction gratings to collimate the beam after achieving spatial dispersion (Figure 3-3). Both of the diffraction gratings have uniform groove density of 2200 lines/mm which produces collimated 1D rainbow beam, mapping each wavelength into space along the 1D line. It is well-known that depending on the polarization of the pulse, the diffraction efficiency changes. Problem arises when the polarization of the pulse drifts over time. The pulse with uncontrolled polarization will result in non-uniform beam profile along the 1D line as can be seen in the Figure 3-3 (c). The issue can be avoided by installing waveplates before the diffraction grating and controlling the polarization of the pulse.
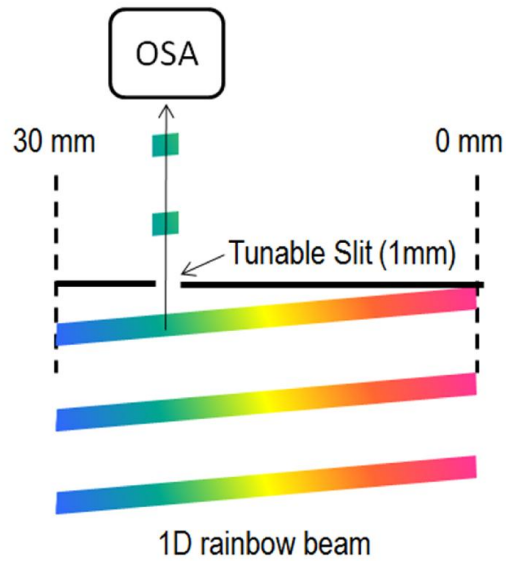
Figure 3-4. Schematic of space-wavelength conversion experiment. A portion of the rainbow beam is selected by a tunable slit where its wavelength is measured by optical spectrum analyzer (OSA). Position of the tunable slit and the wavelength measured by OSA is recorded in pair.

To determine the characteristic of conversion between wavelength and space, we have performed an experiment by placing a tunable narrow slit after the diffraction grating. As the Figure 3-4 illustrates, we select out 1 mm width of the 1D rainbow beam and find the corresponding peak wavelength by optical spectrum analyzer. We then shift the tunable slit to find the wavelength and space relationship by sweeping over the entire range. The result is shown in Figure 3-5.
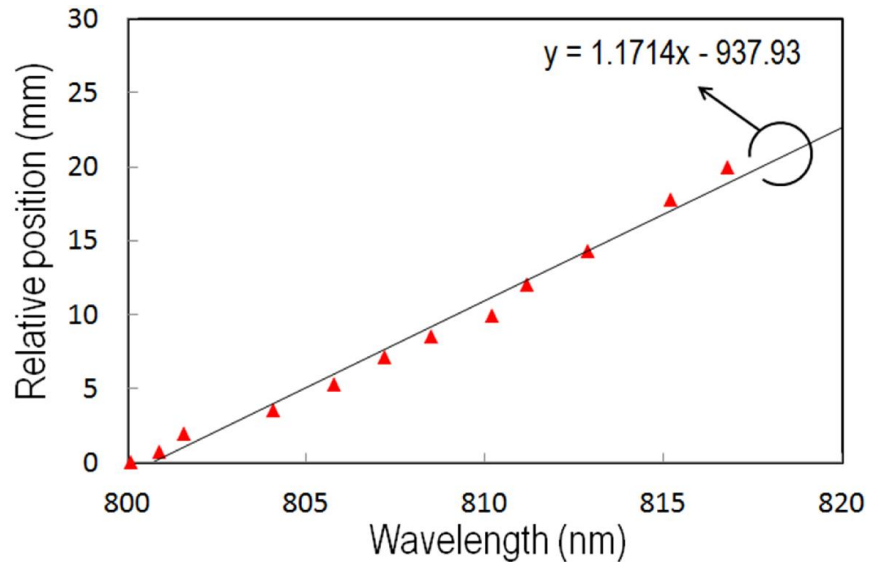
Figure 3-5. Space-wavelength relationship. Data set is fitted by linear function which its slope represents space-wavelength conversion factor (1.1714 mm/nm)

We have fitted the result into a linear function which has a slope of 1.1714 mm/nm. Here, space-wavelength conversion factor C_x is equal to the slope of the linear fit. The conversion factor will be used in later section for analyzing the performance of the system.

3.4 Sample

The sample substrate for our dark-field web inspection system requires clear surface. Also to examine the detection sensitivity of our system, we need to place defects in the scale of 10 μm × 10 μm in size. The sample substrates that we found suitable for the experiment were (1) flexible film and (2) hard-disk cylinder. On top of these substrates, we have placed two types of defects metallic ink and puncture with a micro-needle.

In order to have a flexible film with clear surface we have cured PDMS on top of square-shaped absorptive film (Kodak Wratten 2) as shown in Figure 3-6 (a, b). The dimension of the film was set as 5 cm × 5 cm to avoid rainbow beam (3 cm wide) being incident onto different region than the sample.
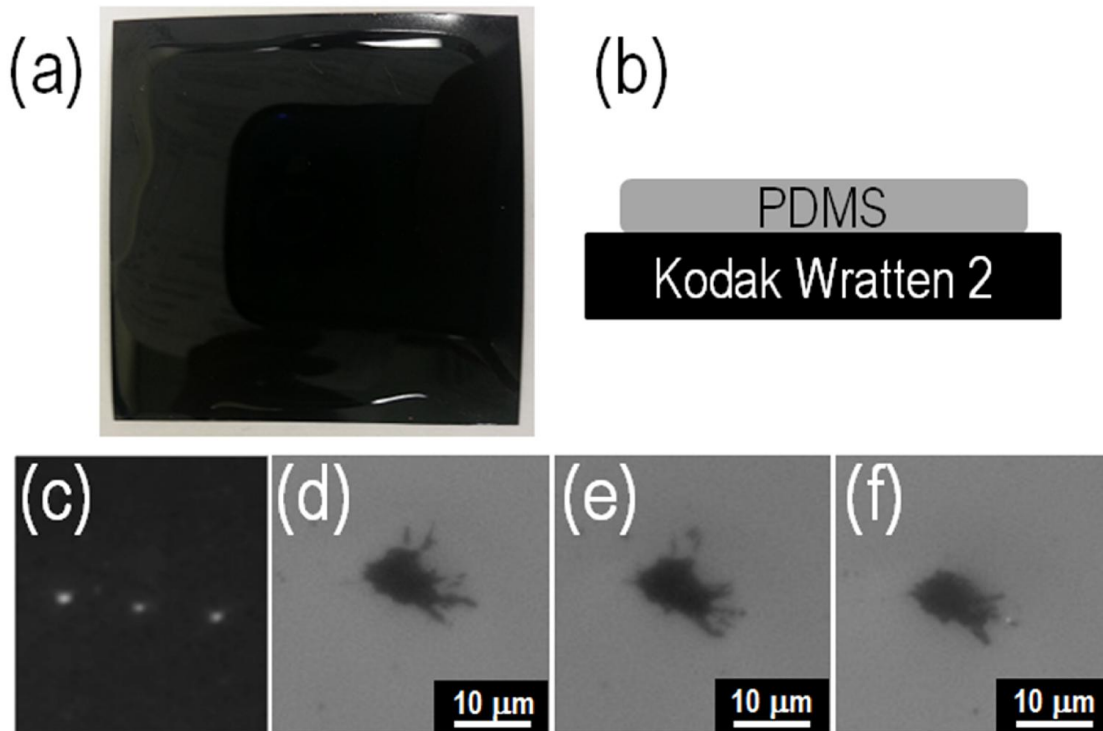
Figure 3-6. (a) PDMS covered absorptive film (Kodak Wratten 2). (b) Side-view of the film sample. (c) CMOS camera image of three 10 μm × 10 μm sized defects. (d,e, and f) Microscope image (10x) of the three defects.

The PDMS covered sample is punctured with a micro-needle (Roboz Surgical) having less than 3 μm of tip diameter. As the Figure 3-6 (d,e, and f) shows, the area of the defects are less than 100 μm². The sample is then mounted on the rotary roller provided by Hitachi Corporation (Figure 3-7). The maximum velocity of the roller is 3 m/s with the accuracy of 10 μm where the sample stays intact with the roller by vacuum force.
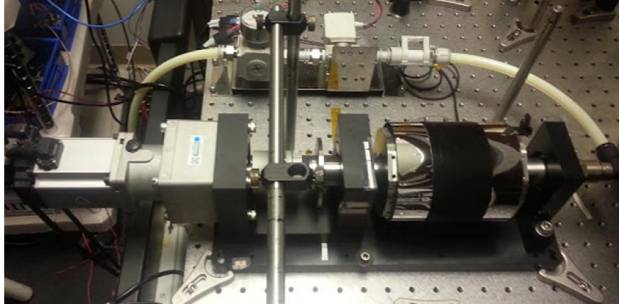
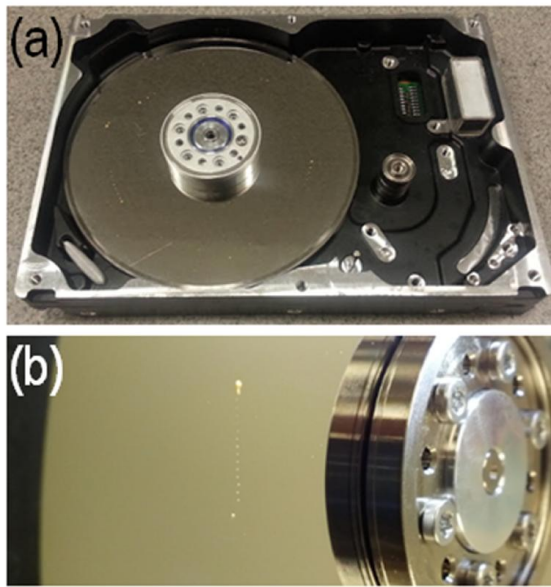Figure 3-7. Rotary roller provided by Hitachi, Ltd. with maximum velocity of 3 m/s

Figure 3-8. (a) Hard-disk sample, (b) 15 defects with size in the scale of 10 μm × 10 μm placed on the hard-disk cylinder

To demonstrate the high-speed inspection capability, we have also used hard-disk cylinder as a test substrate. Its rotational speed is given as 7200 rpm where the metallic ink defects are located 3 cm away from the center. This can be translated into linear speed of 22.62 m/s far exceeding the rotary roller speed.

3.5 Photodetector

In order to detect scattered light from the defect, we need a photodetector module that is sensitive to very weak light. Basic knowledge of the photodetector is crucial in the initial

building stage of the system because of its high sensitivity and fragile nature. The photodetector that we use in the system is photomultiplier tube (PMT) and hybrid photodetector (HPD). This section will briefly cover the basic operating principles of the PMT and the HPD and analyze the response characteristics [23].

PMT consists of a photocathode, focusing electrodes, an electron multiplier (dynodes), and an anode which are all cased inside of a vacuum tube. The procedure of generating an output signal from input light starts with light hitting the photocathode. Through photoelectron emission, the electrons are emitted towards the inner vacuum tube from the photocathode. The focusing electrode guides the electrons onto the dynode where the electrons are multiplied by secondary electron emission. Cascaded dynodes will repeat the multiplying process of electrons and finally collected by the anode.
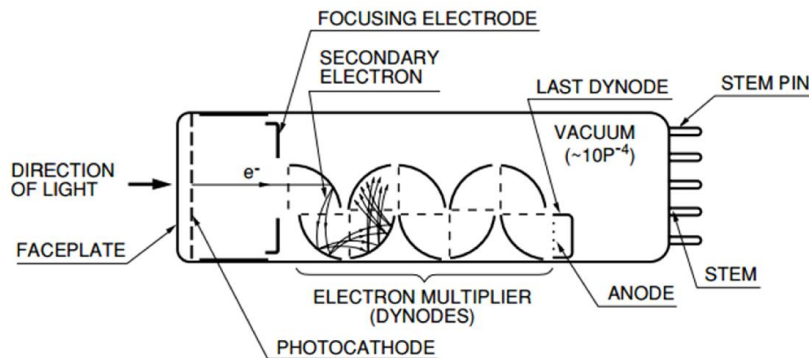

Figure 3-9. Schematic of Photomultiplier tube (PMT) [23]

HPD has a photocathode which generates photoelectrons from the incident light and an avalanche diode with reverse bias voltage applied. The photoelectrons generated from the photocathode are accelerated by a kilovolt-scale electric field. The accelerated electrons are bombarded onto the avalanche diode where electron-hole pairs are generated corresponding to the incident energy of the photoelectrons. Multiple electron-hole pairs that are generated by bombardment results in signal gain which is called an electron bombardment gain. The avalanche diode offers another stage of gain which is known as avalanche gain. Due to its

simplicity in structure, HPD has its merit in multiple aspects; stability, less afterpulse (spurious pulses), better pulse height resolution and high collection efficiency are noticeable characteristics. However, gain of the HPD is generally lower than that of PMT therefore it requires compensation by using additional RF amplifier to achieve desired signal level.
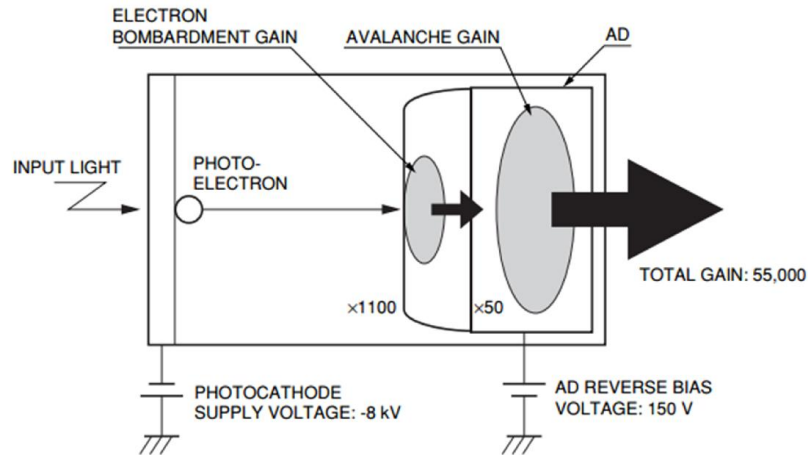

Figure 3-10. Schematic of Hybrid photodetector (HPD) [23]

Both PMT and HPD have rise and fall time shorter than 5 ns which is sufficient enough to resolve scattered signals within 11 ns of temporal window.

We have acquired response function of the PMT from the thermally generated electron as below. The rise time of our PMT is 500 ps which correspond well with the documented value of 570 ps. It is understood that ripples (secondary pulses) after the main pulse arises because of varying electron trajectory inside the PMT.
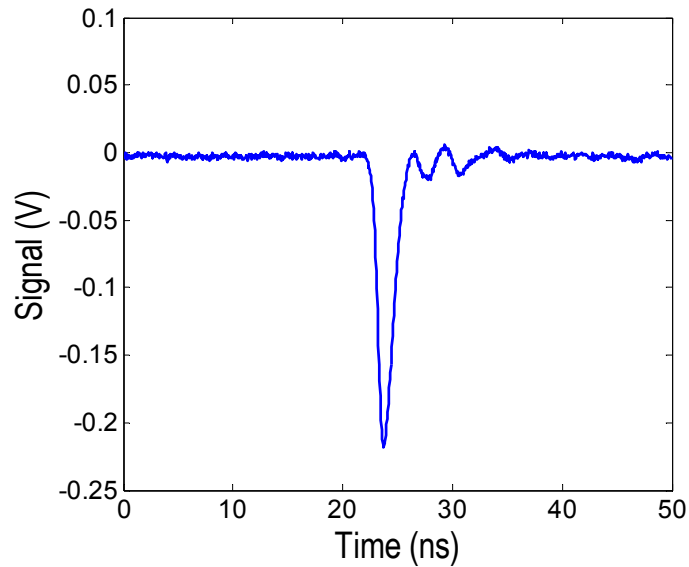
Figure 3-11. Response function of the PMT

3.6 Oscilloscope and Image reconstruction

20GS Tektronix oscilloscope which is able to capture data with the temporal resolution of 50 picosecond per point, is used in our system. The sampling rate of our oscilloscope is much higher than the bandwidth of the photodetector module; therefore the oscilloscope is not a factor that limits our system.

Data acquired from the oscilloscope is then processed through Matlab code which reconstructs the inspection image. It is required that we record the laser trigger signal along with the PMT signal. This is explained in the Figure 3-12, where a ">" shaped defect is passing through the rainbow beam that is performing the line scan. Regarding that the red part of the rainbow hits the defect prior to the blue part, the scattered signal from red part will be recorded earlier than the signal coming from the blue part. As it can be seen from the Figure 3-12 (a), the laser trigger will signal the start of the line scan and the end of the line scan. Based on this trigger signal, window for each vertical slice of the resulting image is assigned. PMT signals between two trigger signal will be arranged in a vertical manner within the frame as shown in Figure 3-12 (b). The PMT signal peak in the Figure 3-12 (b) is

28

marked as a solid black dot. Rearranging every signal peak as described, we are able to reconstruct the image for the ">" shaped defect.
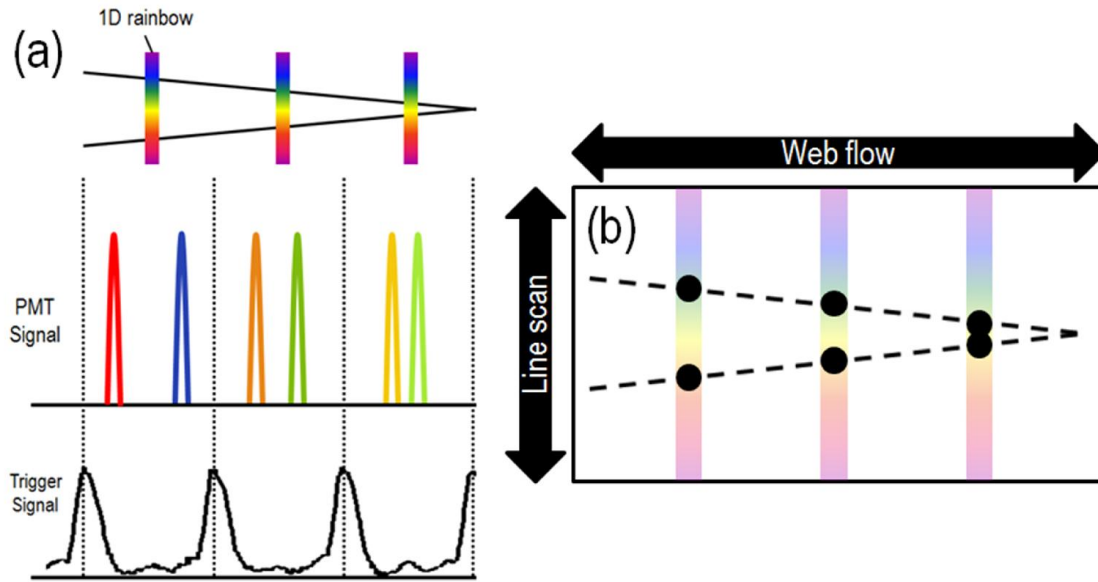

Figure 3-12. Description of PMT and trigger signal during line scan. (a) shows rainbow beam incident onto ">" shaped defect and corresponding PMT signal and trigger signal at three different time instant. (b) demonstrates how image frame is generated from the PMT signal and the trigger signal.

Chapter 4 Results and performance analysis

In this chapter, we will show the imaging/inspection result for the flexible film and the hard-disk cylinder samples. Also, performance of the system will be theoretically analyzed followed by the results. Prior to presenting reconstructed image results, we will briefly analyze acquired raw data for three different samples shown in Figure 4-1, 4-2, and 4-2 respectively.
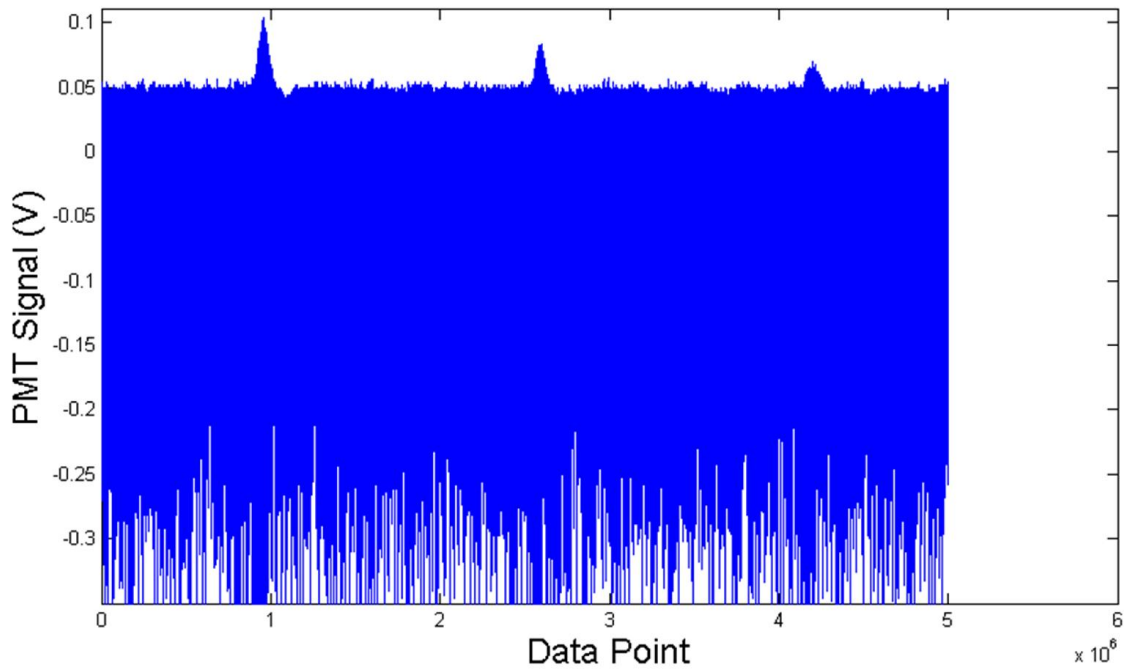
Figure 4-1. Raw data for three 10 μm × 10 μm defects on PDMS covered film

It is important to note that the three positive peaks shown in the Figure 4-1 are due to baseline shifting of the PMT. The actual line scan information is in the negative portion of the signal. The signal on the negative side is hard to distinguish because of the background noise from the sample is higher than the following two experiment.
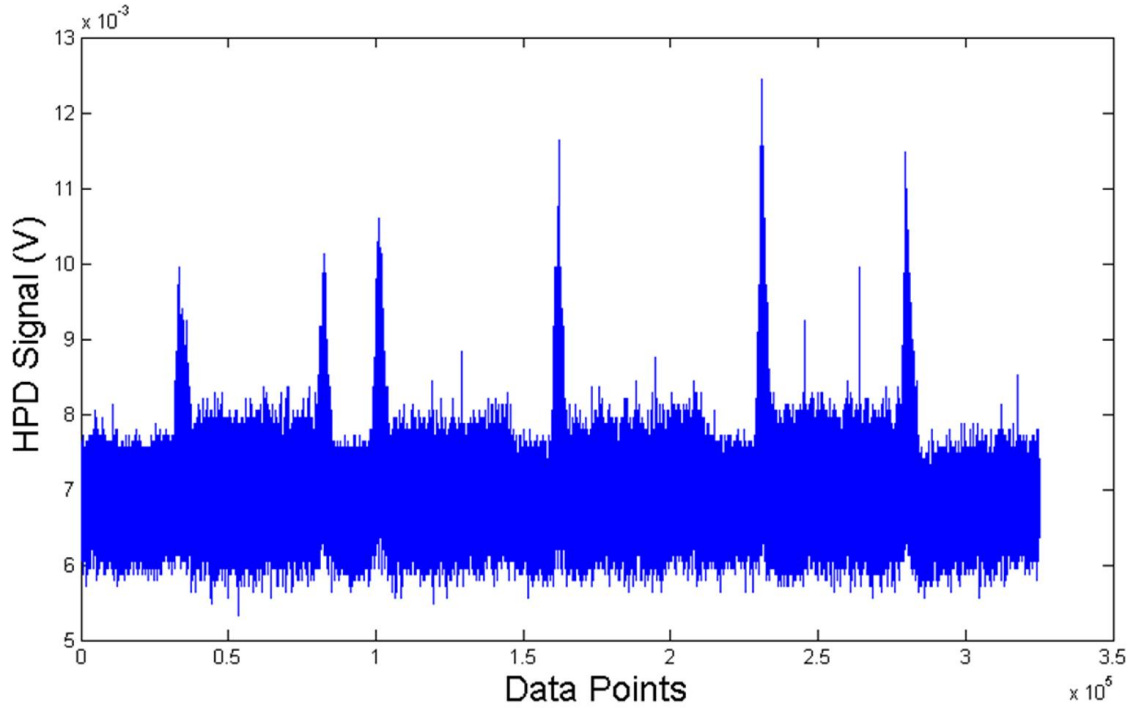
Figure 4-2. Raw data for "UCLA" defect on absorptive film

The four distinct features in Figure 4-2 each corresponds to U, C, L, and A respectively. Since we have used HPD for this experiment, the signal response in the positive direction is noticeable. Also, we may notice that the signal voltage is comparably smaller than that of the PMT's. Despite that the scale of the defects are much larger than 10 μm × 10 μm punctured defects, signal voltage is lower due to the HPD's lower gain characteristic.

Figure 4-3. Raw data for fifteen defects on the hard-disk cylinder sample

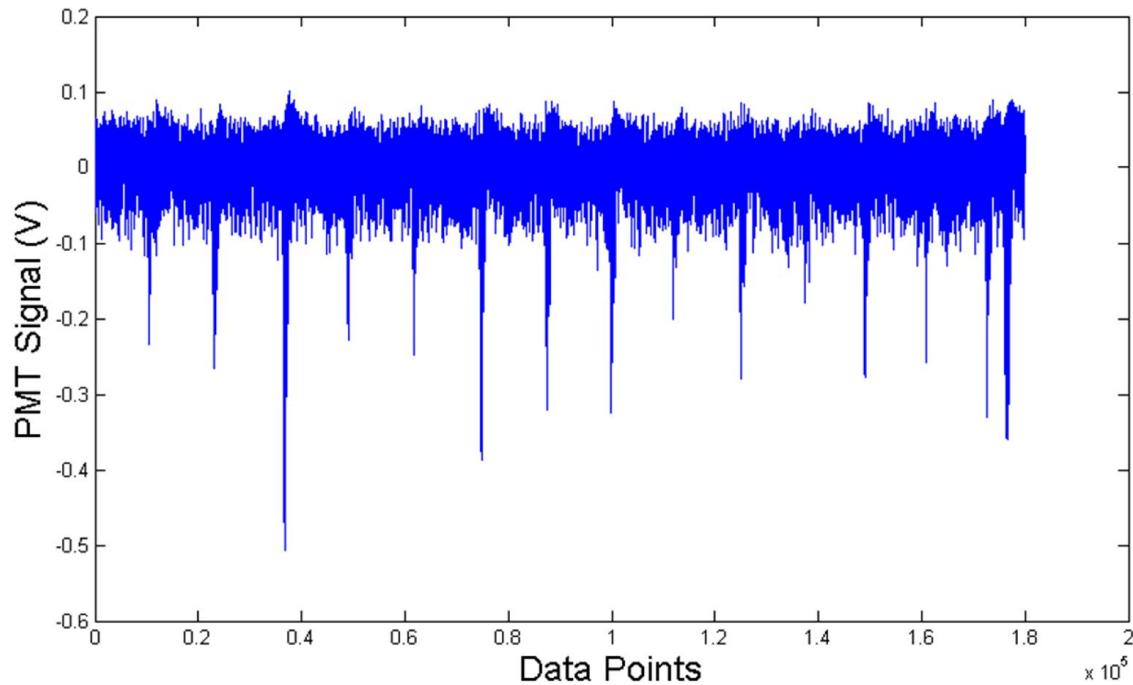The defect signal coming from hard-disk cylinder is very much distinguishable because of the cylinder's clean surface. We can clearly observe fifteen evenly-spaced defects where the baseline shift is less than the previous samples. Relationship between size of each defect and their corresponding peak voltage did not show correlation. We may assume that the defect texture in microscopic scale were not uniform. Thus the scattering characteristic may depend more on their texture than their size. The following section will show reconstructed inspection result based on the raw data given above.

4.1 Results: film sample on rotary roller

Mentioned in the previous section, the absorptive film surface is coated with PDMS where the defects are placed by puncturing through the PDMS layer. Figure 4-4 (a) is a photo of 10 μm sized defects acquired by CMOS camera. After the image reconstruction, we have successfully identified the three defects on the film as can be seen in Figure 4-4 (b).

32
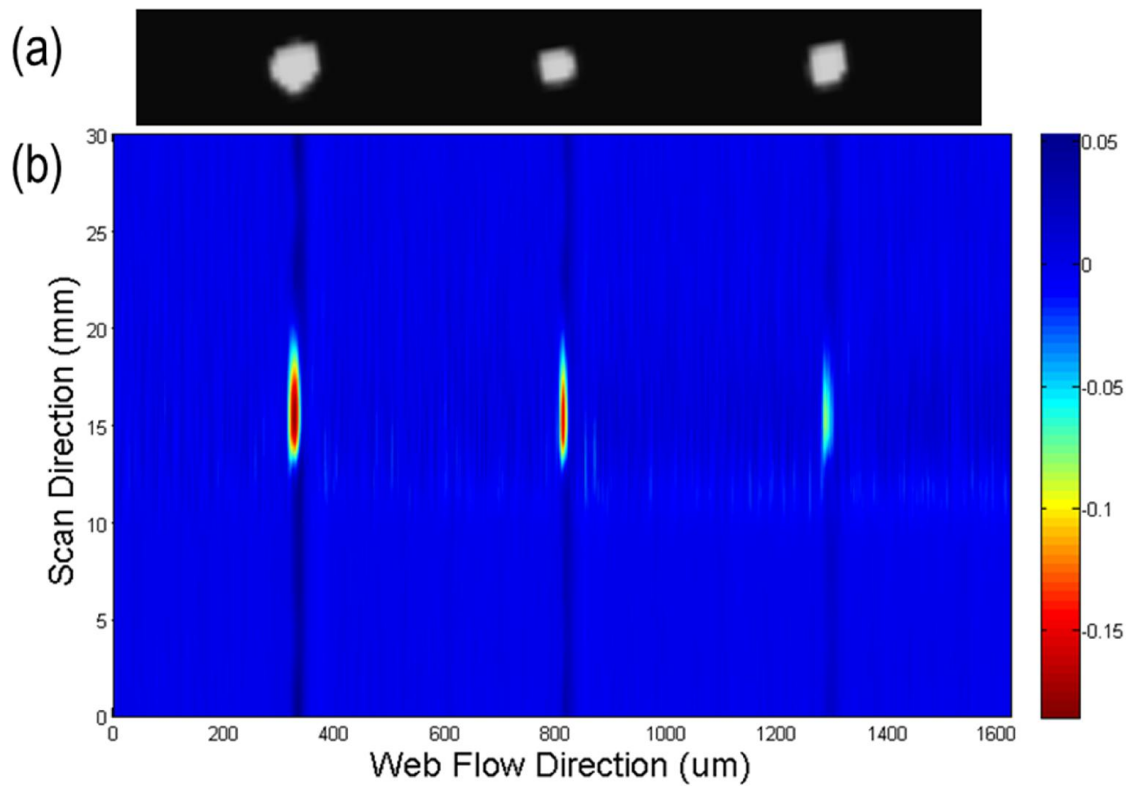
Figure 4-4. (a) CMOS camera image of three defects on the film sample and (b) corresponding line scan result from the three defects

One of the features in this figure is that there are vertical lines visible along the defect location. This is an artifact coming from the PMT characteristic where high intensity light may shift the base-line of the PMT signal. The CMOS camera image of the defects looks larger than its actual size because of the limited resolution in the CMOS camera. The base-line shift can be readily seen in the vertically sliced plot. Figure 4-5 (b) and (c) are signal from the defect and clear surface respectively. Figure 4-5 (b) has the base-line of around 0.03 V whereas Figure 4-5 (c) has 0 V.
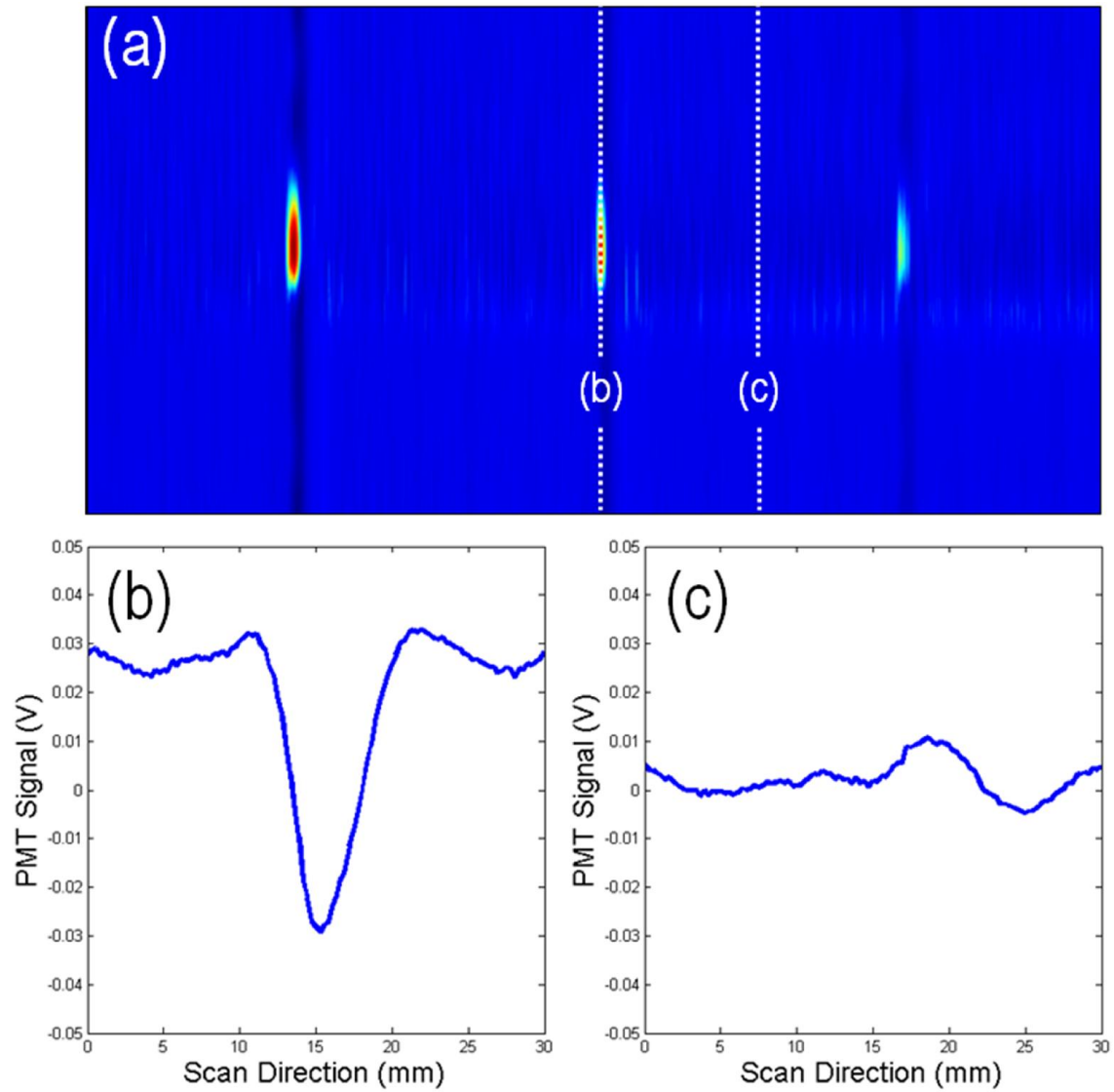
Figure 4-5. Comparison of PMT signal at different locations. (a) shows the location of vertical slice for signal (b) and (c). (b) PMT signal from the defect. (c) PMT signal from the clear surface.

We have also performed a test with "UCLA" defect which is written with metallic ink on the absorptive film. A photo of the sample is shown in Figure 4-6. Again, the roller speed is set as 3 m/s. We have used HPD instead of PMT for this experiment because the HPD has shorter rise and fall time characteristics. With faster response time, we are able to reconstruct the image with better spatial resolution. However, we need to note that the sensitivity of the

HPD is significantly lower than the PMT. Here, lower sensitivity does not affect our experiment since the defect size is relatively bigger than the previous 10 μm defect inspection.

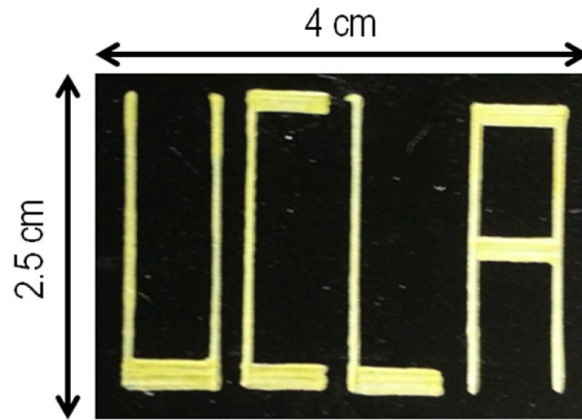Figure 4-6. "UCLA" written on film sample with metallic ink

The result of inspection is shown in the figure below. Figure 4-7 (a) and (b) clearly shows the character "UCLA" with different color coding. We can observe the blurring of the characters in the vertical direction which is due to our spatial resolution limit in line scan direction. The detailed explanation will be followed in the performance analysis section.
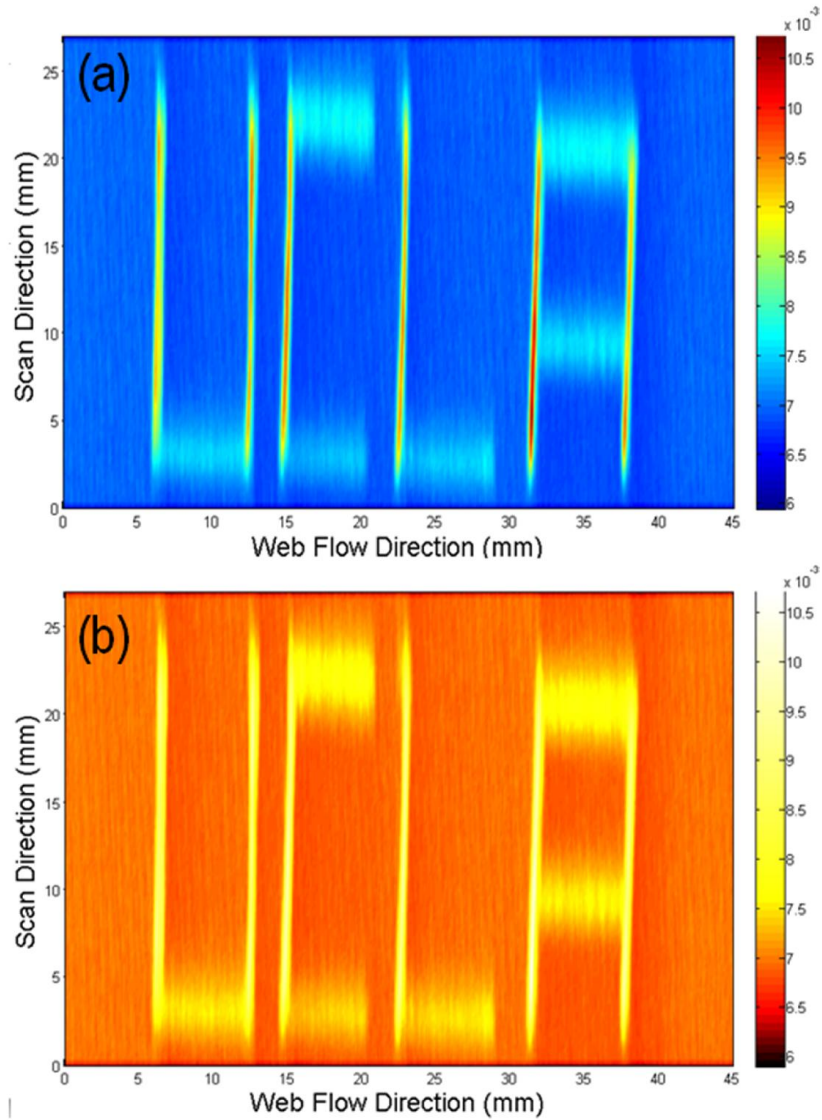
Figure 4-7. Line scan result from the UCLA-written film sample. (a) "jet" color-coded plot (b) "hot" color-code plot

4.2 Results: hard-disk cylinder sample

Fifteen defects on the hard-disk cylinder with sizes ranging from 10 μm × 10 μm to 20 μm × 20 μm were inspected while the cylinder rotating at speed of 7200 rpm. Figure 4-8 shows the defect dimensions and their location. The defects are arranged in a single line where they are shown in Figure 4-8 (a). Microscope image of each defects are given in Figure 4-8 (b) with the scale bar.
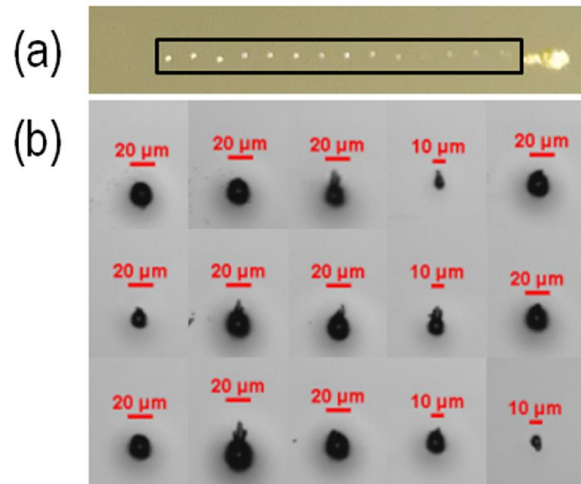
Figure 4-8. Defect image taken by (a) CMOS camera and (b) microscope

The inspection result of the fifteen defects on hard-disk cylinder is as below (Figure 4-9 and Figure 4-10). Again, for this experiment, we have used the PMT with high gain due to the fact that the sizes of the defects are in the scale of micrometers. In Figure 4-9 (b) we have used rotation angle as our x-axis since the web flow speed is different depending on its position.
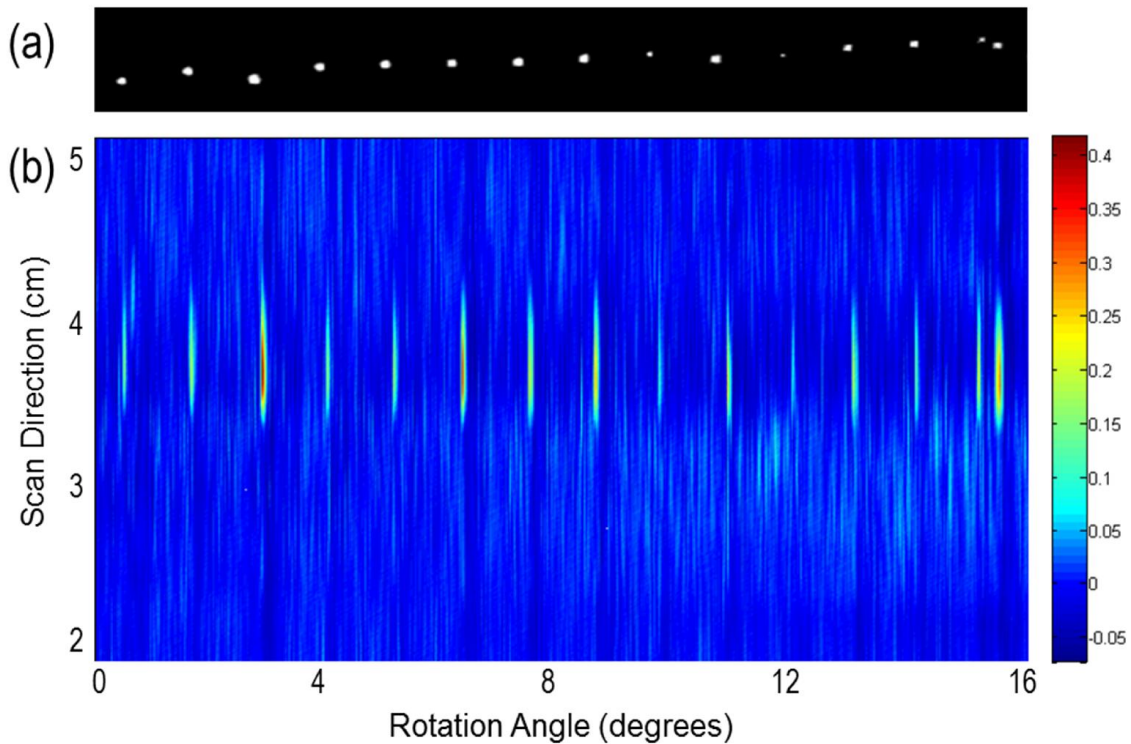
Figure 4-9. (a) CMOS camera image of 15 defects on the hard-disk cylinder (b) line scan result of 15 defects on hard-disk cylinder rotating at speed of 7200 rpm
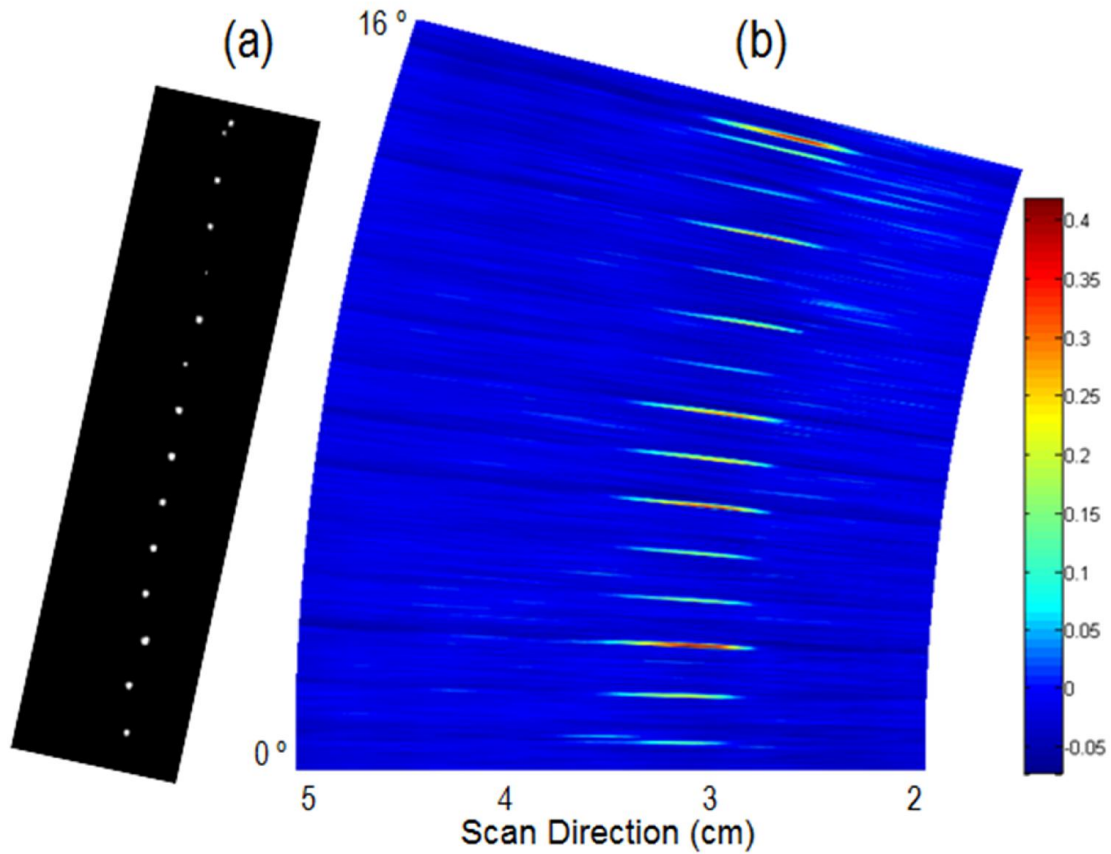
Figure 4-10. (a) CMOS camera image of 15 defects on the hard-disk cylinder (b) Line scan result of 15 defects plotted in polar coordinate

In this section, we have shown inspection results for (1) flexible film and (2) hard-disk cylinder samples.

4.3 Performance of the web inspection system

In this section, we will investigate the theoretical performance of the system including scan rate and spatial resolution in two directions: web flow direction and scan direction.

The scan rate, R is given as the pulse repetition rate of the laser system since a single pulse can complete a line scan. Spatial resolution in web flow direction is equivalent to the beam width of the 1D rainbow beam. Here the maximum speed of the web is imposed where it can

be calculated by multiplying beam width in the flow direction by the scan rate R. However, in most cases the maximum speed is limited by the translation device as the theoretical maximum speed for our system is given as 1.8 km/s.

Spatial resolution of the system is not only determined by diffraction limit as conventional microscopy, but also by the characteristics of the temporal and spatial dispersion elements. Evaluation of the spatial resolution in line scan direction needs consideration of three main factors: (1) the spectral resolution determined by DFT with stationary-phase-approximation (SPA), (2) the spectral resolution of the spatial disperser and (3) the temporal resolution of the digitizer [24]. Each of these elements imposes their own spatial resolution limit and the combination of all three factors will give us the resolution of the whole system.

First, we analyze the spectral resolution limit in the process of DFT. In ideal DFT, one-to-one wavelength-time mapping should occur. In other words, at certain time within the DFT processed pulse, there should be only one wavelength occupying that time instant. However, due to the nature of the DFT such discrete wavelength-time mapping cannot be achieved. This ambiguity arises specifically because of stationary-phase-approximation (SPA) employed in DFT and its spectral resolution limit can be expressed as, [18, 24]

$$\delta\lambda_{SPA} = \lambda_0 \sqrt{\frac{2}{D \cdot c}}.$$

(26)

Here, D is the group-velocity dispersion without the high-order dispersion and c is the speed of light. The spatial resolution imposed by $\delta\lambda_{SPA}$ is,

$$\delta x_{SPA} = C_x \cdot \delta\lambda_{SPA},$$

(27)

where C_x represents the space-wavelength conversion factor which is covered in Chapter 3.

The space-to-wavelength mapping is achieved by the diffraction grating. Assuming first-order diffraction, the spectral resolution from the diffraction grating is given as, [25]

$$\delta\lambda_g = \frac{\lambda_0 \cdot d \cdot \cos\theta_g}{W}.$$

(28)

Here, θ_g is the diffracted angle, d is grating period, λ_0 is the center wavelength, and W is the waist of the incident beam. From the above condition, the grating limited spatial resolution $\delta x_{grating}$ can be expressed as,

$$\delta x_{grating} \approx C_x \cdot \delta\lambda_g.$$

(29)

Secondly, the detection system (i.e., photomultiplier tube and oscilloscope) with finite bandwidth limits the spatial resolution of the system. The temporal resolution or rise time of the digitizer is converted to corresponding spectral resolution as below [18, 24].

$$\delta\lambda_{det} = \frac{\tau_{det}}{D} = \frac{0.35}{D \cdot f_{det}}.$$

(30)

Here τ_{det} and f_{det} are the rise/fall time and bandwidth of the detection system respectively (i.e., the PMT and oscilloscope). The spatial resolution limit by digitizer then can be expressed as,

$$\delta x_{det} = C_x \cdot \delta\lambda_{det}.$$

(31)

We combine all three factors of spatial resolution δx_{SPA}, $\delta x_{grating}$, δx_{det} for the whole system and the overall spatial resolution is determined as,

$$\Delta x = \max(\delta x_{SPA}, \delta x_{grating}, \delta x_{det}).$$

(32)

Our system is limited by the detection system, where $\delta x = \delta x_{det} \approx 5.265$ mm. Therefore the spatial resolution in line scan direction is given as 5.265 mm. However within a line scan,

the web inspection system is able to capture defect size less than the resolution. We have calculated detectable resolution of the system which is governed by the digitzer's sampling rate, as 136 μm/pixel. Despite that the defect scattered signal may be broadened in the line scan direction (image is blurred), assuming sparse defect distribution, the peak location of the scattering signal tells us the location of the defect with precision of 136 μm. The spatial resolution in web flow direction is 20 μm which is the beam width of the rainbow.

Chapter 5 Future Work and Conclusion

5.1 Future Work

Our system can be immediately improved by utilizing acousto-optic modulator and non-imaging collection optics. These components are conventionally available and its implementation to our system is realistic.

First, the spatial resolution of our inspection system is currently limited by optical detection speed. In other words, the number of sample points within the dispersed pulse is limited. To overcome the limitation we may use photodetector with higher speed or introduce higher temporal dispersion. As the higher speed photodetector is costly in many ways, the second option is more appreciable. Pulse with a larger temporal dispersion will allow us to have more sample points with the same detector speed. However, we have an upper limit for temporal dispersion where the pulse repetition rate determines the maximum temporal dispersion amount (Chapter 3). Among various methods to change the pulse repetition rate (i.e., cavity dumper, longer cavity length, modulator-based pulse picker), we may use the most simple technique. By using acousto-optic modulator as a pulse picker, we can decrease the pulse repetition rate. This enlarges the window to support larger temporal dispersion while avoiding overlap between consecutive pulses.

Secondly, we may further enhance the spatial resolution in the line scan direction with additional signal processing. Starting from the impulse response of the photodetector (Figure 3-11), we deconvolute the acquired signal train in time domain. This is equivalent to equalization process in frequency domain and results in narrower signal in temporal domain. Therefore reconstruction of an image with the deconvoluted signal train will have higher spatial resolution in line scan direction which is the direction of deconvolution. This however, requires sparse distribution of defects where multiple scattered signals within a line scan may drive the photodetector module away from its linear response regime resulting in distorted image.

Finally, non-imaging collection optics will efficiently capture the scattered light coming from the defect. With the collection optics we may drastically expand our field-of-view and improve the signal-to-noise ratio and the sensitivity of the system.

5.2 Conclusion

In conclusion, we have confirmed that we were able to show web inspection results with up to 20 m/s of web flow speed. The inspection was performed in real-time, while successfully detecting the defects that are less than 10 μm × 10 μm in size. Theoretical maximum web-flow speed is determined as 125 km/min which we were not able to demonstrate because of speed limitation of our translational device. The detectable resolution of the system is 136 μm/pixel; the spatial resolution is 5.265 mm in the line scan direction and 20 μm in the web flow direction.

The study presented the principle of high throughput web inspection system for fast real-time line scan. The novel technique, photonic time-stretch (or dispersive Fourier transformation), employed in the system was described in detail supported by mathematical derivation. Furthermore, important elements in the system are explained while connecting them to the goal of this thesis.

The demonstrated system with unprecedented scanning speed has its application in quality control for various manufacturing fields such as turbine propellers, turbo pumps, and train track inspection. Its capability of inspecting with ultrafast speed will be more appreciated in the future since the production yield is continuously increasing in many manufacturing sectors.

REFERENCES

1.   Bhushan, A.S., F. Coppinger, and B. Jalali, *Time-stretched analogue-to-digital conversion*. Electronics Letters, 1998. **34**(9): p. 839-841.

2.   Chou, J., et al., *Femtosecond real-time single-shot digitizer*. Applied Physics Letters, 2007. **91**(16).

3.   Chou, J., D.R. Solli, and B. Jalali, *Real-time spectroscopy with subgigahertz resolution using amplified dispersive Fourier transformation*. Applied Physics Letters, 2008. **92**(11).

4.   Goda, K., K.K. Tsia, and B. Jalali, *Serial time-encoded amplified imaging for real-time observation of fast dynamic phenomena*. Nature, 2009. **458**(7242): p. 1145-U80.

5.   Han, Y. and B. Jalali, *Photonic time-stretched analog-to-digital converter: Fundamental concepts and practical considerations*. Journal of Lightwave Technology, 2003. **21**(12): p. 3085-3103.

6.   Goda, K., et al., *Hybrid Dispersion Laser Scanner*. Scientific Reports, 2012. **2**.

7.   Buckley, B.W., A.M. Madni, and B. Jalali, *Coherent time-stretch transformation for real-time capture of wideband signals*. Optics Express, 2013. **21**(18): p. 21618-21627.

8.   Chen, H.W., et al., *Ultrafast web inspection with hybrid dispersion laser scanner*. Applied Optics, 2013. **52**(17): p. 4072-4076.

9.   Tsai, D.M. and T.Y. Huang, *Automated surface inspection for statistical textures*. Image and Vision Computing, 2003. **21**(4): p. 307-323.

10.   Olsson, L.J. and S. Gruber, *Web Process Inspection Using Neural Classification of Scattering Light*. Ieee Transactions on Industrial Electronics, 1993. **40**(2): p. 228-234.

11.   Sorebo, J.H. and R.D. Lorenz, *Web inspection using gradient-indexed optics*. Ieee Transactions on Industry Applications, 2005. **41**(6): p. 1476-1482.

12.   Son, S., H. Park, and K.H. Lee, *Automated laser scanning system for reverse engineering and inspection.* International Journal of Machine Tools & Manufacture, 2002. **42**(8): p. 889-897.

13.   Goda, K. and B. Jalali, *Dispersive Fourier transformation for fast continuous single-shot measurements.* Nature Photonics, 2013. **7**(2): p. 102-112.

14.   Wikipedia, *Time stretch dispersive Fourier transform.* 2013.

15.   Jannson, T., *Real-time Fourier transformation in dispersive optical fibers.* Optics Letters, 1983. **8**(4): p. 232-234.

16.   Azana, J. and M.A. Muriel, *Real-time optical spectrum analysis based on the time-space duality in chirped fiber gratings.* Ieee Journal of Quantum Electronics, 2000. **36**(5): p. 517-526.

17.   Kolner, B.H., *Space-Time Duality and the Theory of Temporal Imaging.* Ieee Journal of Quantum Electronics, 1994. **30**(8): p. 1951-1963.

18.   Goda, K., et al., *Theory of amplified dispersive Fourier transformation (vol 80, 043821, 2009).* Physical Review A, 2010. **81**(3).

19.   Goda, K., A. Mahjoubfar, and B. Jalali, *Demonstration of Raman gain at 800 nm in single-mode fiber and its potential application to biological sensing and imaging.* Applied Physics Letters, 2009. **95**(25).

20.   Headley, C. and G.P. Agrawal, *Unified description of ultrafast stimulated Raman scattering in optical fibers.* Journal of the Optical Society of America B-Optical Physics, 1996. **13**(10): p. 2170-2177.

21.   Goda, K., et al., *High-throughput single-microparticle imaging flow analyzer.* Proceedings of the National Academy of Sciences of the United States of America, 2012. **109**(29): p. 11630-11635.

22.   Mahjoubfar, A., et al., *High-speed nanometer-resolved imaging vibrometer and velocimeter.* Applied Physics Letters, 2011. **98**(10).

23.   Photonics, H., *Photomultiplier Tubes: Basics and Applications.* 2006.

24. Tsia, K.K., et al., *Performance of serial time-encoded amplified microscope*. Optics Express, 2010. **18**(10): p. 10016-10028.

25. Tearney, G.J., M. Shishkov, and B.E. Bouma, *Spectrally encoded miniature endoscopy*. Optics Letters, 2002. **27**(6): p. 412-414.